The magnetic field and stellar wind of the mature late-F star χ Draconis A

S. C. Marsden [1]★, D. Evensberget [1,2]★, E. L. Brown [1], C. Neiner [3], J. M. Seach [1], J. Morin [4], P. Petit,[5] S. V. Jeffers[6] and C. P. Folsom[7,8]

[1] *Centre for Astrophysics, University of Southern Queensland, Toowoomba 4350, Australia*
[2] *Leiden Observatory, Leiden University, PO Box 9513, NL-2300 RA Leiden, the Netherlands*
[3] *LESIA, Paris Observatory, PSL University, CNRS, Sorbonne University, Université Paris Cité, 5 place Jules Janssen, F-92125 Meudon, France*
[4] *Laboratoire Univers et Particules de Montpellier, Université de Montpellier, CNRS, F-34095 Montpellier, France*
[5] *Institut de Recherche en Astrophysique et Planétologie, Université de Toulouse, CNRS, CNES, 14 avenue Edouard Belin, F-31400 Toulouse, France*
[6] *Max-Planck-Institut für Sonnensystemforschung, Justus-von-Liebig-Weg 3, D-37077 Göttingen, Germany*
[7] *Tartu Observatory, University of Tartu, Observatooriumi 1, Tõravere, 61602 Tartumaa, Estonia*
[8] *Department of Physics & Astronomy, University of Western Ontario, London, ON N6A 3K7, Canada*

ABSTRACT

F stars lie in the transition region between cool stars with dynamo generated fields and hot star fossil fields and offer an interesting window into the generation of magnetic fields in shallow convection zones. In this paper, we investigate the magnetic field of the mature F7V primary of the bright χ Draconis system. χ Dra was observed in circularly polarized light at four epochs from 2014 through to 2019 using the NARVAL spectropolarimeter at the Télescope Bernard Lyot. Using the technique of least-squares deconvolution, we created high signal-to-noise line profiles from which we were able to measure the radial velocity of both the primary and secondary and use these to improve the orbital parameters of the system. Additionally, we used the technique of Zeeman Doppler imaging to reconstruct the large-scale magnetic field geometry of the primary at the four epochs. The magnetic maps show that χ Dra A has a predominately dipolar poloidal magnetic field at all epochs with the magnetic axis well aligned with the stellar rotation axis. The large-scale features of the magnetic field appear to be relatively stable over the ∼5 yr time base of our observations, with no evidence of any polarity reversals. We used the magnetic field maps to model the wind from χ Dra A at all epochs, showing that the mass-loss from the stellar wind of χ Dra A is 3–6 times the current solar value, while the angular momentum loss from the wind is around 3–4 times the solar value.

Key words: stars: activity – binaries: spectroscopic – stars: individual: (χ Dra) – stars: magnetic fields.

1 INTRODUCTION

The generation of magnetic fields is an important process operating inside solar-type stars that can influence everything from the star's rotational evolution (e.g. Weber & Davis 1967; Mestel 1968; Skumanich 1972; Soderblom, Jones & Fischer 2001; Matt et al. 2012; Bouvier et al. 2014; Gallet & Bouvier 2015; Garraffo et al. 2018; See et al. 2018; Shoda et al. 2020; Metcalfe et al. 2022) through to the habitability of any orbiting planets (e.g. Lammer et al. 2010; See et al. 2014; Garraffo, Drake & Cohen 2016; Gallet et al. 2017; Johnstone et al. 2019; Airapetian et al. 2020; Vidotto & Cleary 2020; Evensberget et al. 2021, 2022; Ridgway et al. 2023). Solar-type star magnetic fields are considered to be generated by dynamo processes in their outer convective layer, with most, if not all, solar-type stars having some level of magnetic field (e.g. Landstreet 1992; Baliunas et al. 1995; Berdyugina 2005; Hall 2008; Donati & Landstreet 2009; Reiners 2012; Marsden et al. 2014; Brun & Browning 2017). Such dynamo generated magnetic fields usually show complex and

evolving structures and potentially cyclic behaviour as is observed on the Sun (e.g. τ Boötis, Mengel et al. 2016; Jeffers et al. 2018; HD 75332 Brown, et al. 2021; and 61 Cyg A, Boro Saikia et al. 2016), with these evolving magnetic fields offering a window into the operation of the stellar dynamo (e.g. Jeffers et al. 2022).

In contrast to this are the magnetic fields on hotter stars, which do not have an outer convective layer, and where approximately only 5–10 per cent of such stars host a fossil field (e.g. Donati & Landstreet 2009; Grunhut, Wade & MiMeS Collaboration 2012; Fossati et al. 2015; Grunhut & Neiner 2015; Wade et al. 2016; Grunhut et al. 2017; Neiner et al. 2017; Schöller et al. 2017). These fossil fields are generally stronger than dynamo generated fields and are stable on the order of the lifetime of the star (e.g. Donati & Landstreet 2009; Grunhut & Neiner 2015; Alecian et al. 2019). The origin of such fossil fields is still under debate with the possibility that they may be remnant primordial fields from the molecular cloud from which the stars formed or even the frozen field from dynamo generation during the stars' pre-main-sequence evolution (Donati & Landstreet 2009; Neiner et al. 2015; Alecian et al. 2019).

The transition from dynamo generated to fossil magnetic fields is considered to occur somewhere from mid- to early-F spectral type where the outer convection zone thins to a point where a magnetic

dynamo can no longer be supported. The point of transition from dynamo to fossil fields has been based on indirect observations of stellar magnetic activity, such as chromospheric and coronal emission and activity–rotation relationships (e.g. Wilson 1966; Baschek & Reimers 1969; Böhm-Vitense & Dettmann 1980). The exact point of this transition is still not fully known as often F stars are omitted from stellar magnetic field surveys which focus more on either studying the fossil fields of hot stars (e.g. MiMeS, Wade et al. 2016) or the dynamo magnetic fields of cool stars (e.g. BCool, Marsden et al. 2014). Directly observing the magnetic field of F stars is important to understand how magnetic dynamos operate in thinning convection zones and the transition from dynamo generated magnetic fields to fossil fields, but until recently there have been few studies of the properties of the magnetic fields of these stars. In one such study, Seach et al. (2020) looked at the detection of magnetic fields on mature F stars ranging from F0 to F9 and found potentially dynamo generated magnetic fields on stars from F3V to F9V.

The technique of Zeeman Doppler Imaging (ZDI; Semel 1989) allows the mapping of the large-scale magnetic field geometry of stellar surfaces. For young F stars, currently only two have had their magnetic fields mapped using this technique. The young, rapidly rotating late-F star HR 1817 (age ∼25 Myr, Messina et al. 2016; rotational period 0.98 d, Marsden et al. 2006) was studied by Mengel (2005) and Marsden et al. (2006) and was found to host a complex radial magnetic field with a ring of positive azimuthal field around the pole, similar to that seen on a number of young cool stars. The young late-F star HD 35296 (age ∼30–50 Myr, rotational period ∼3.5 d) shows a complex field with a mixture between poloidal and toroidal components (Waite et al. 2015).

For more mature F stars, like χ Dra, there have similarly been few studies. The hot Jupiter hosting star τ Boötis (age ∼1 Gyr, Borsa et al. 2015, rotational period ∼3.31 d) shows a weak and predominantly complex poloidal magnetic field, and an ultrarapid magnetic cycle of ∼240 d (Mengel et al. 2016; Jeffers et al. 2018). There is also strong evidence for a rapid magnetic cycle (∼1.06 yr) for the mature (age ∼1.9 Gyr, Takeda et al. 2007, rotational period ∼3.6 d) F7V star HD 75332, which shows a predominantly simple dipolar poloidal magnetic field at most epochs (Brown et al. 2021). Similarly, the late-F star HD 78366 (rotational period ∼11.4 d) also shows a simple dipolar field at all epochs and rapid field reversals (Morgenthaler et al. 2011), while the hot Jupiter host late-F star HD 179949 (rotational period ∼7.6 d) shows a more complex poloidal magnetic field (Fares et al. 2012). The magnetic field of the mature late-F star β Vir shows simple dipolar poloidal magnetic field topologies while the more rapidly rotating late-F star θ Dra shows more complex fields with the level of poloidal and toroidal field varying between epochs (Seach et al. 2022). Based on this very limited data, it appears that young or more rapidly rotating late-F stars have complex magnetic topologies with a mix between poloidal and toroidal field components while more mature or slower rotating late-F stars have predominantly poloidal and simpler magnetic fields. Three of the observed mature F stars that have multiple epochs of observations (τ Boötis, Mengel et al. 2016; Jeffers et al. 2018; HD 75332, Brown et al. 2021; and HD 78366, Morgenthaler et al. 2011) appear to show extremely rapid magnetic cycles of approximately a few years or even less. Chromospheric cycles (expected to be half the length of a magnetic cycle based on our Sun) of less than a few years have also been observed for a number of F stars (Baliunas et al. 1997; Metcalfe et al. 2010; Mittag et al. 2019; Seach et al. 2022). This makes F stars interesting targets to study magnetic cycles over a reasonably short time frame (compared to the ∼22 yr solar magnetic cycle). Additionally, many of the F stars with observed magnetic

Table 1. Stellar parameters for χ Dra A used/found in this study.

Parameter	Value	Reference
Spectral type	F7 V	Gray, Napier & Winkler (2001)
Stellar mass	$1.00 \pm 0.01\,\mathrm{M_\odot}$	This work
Stellar radius	$1.20 \pm 0.09\,\mathrm{R_\odot}$	Torres et al. (2010)
Stellar rotation period	$23.39 \pm 0.09\,\mathrm{d}$	Lee et al. (2018)
Stellar inclination	$74.42 \pm 0.58^\circ$	Farrington et al. (2010)
$v\sin i$	$2.5 \pm 0.4\,\mathrm{km\,s^{-1}}$	Gray (1984)
Age	∼5 Gyr	Casagrande et al. (2011)
Photospheric temperature	6083 K	Luck (2017)

fields appear to show high levels of surface differential rotation, with values from approximately 3–4 up to ∼10 times the solar differential rotation rate (Mengel 2005; Fares et al. 2012; Waite et al. 2015; Mengel et al. 2016; Brown et al. 2021; Seach et al. 2022).

In this paper, we investigate the large-scale magnetic field of the late-F star χ Draconis A. χ Dra is a binary system whose primary is an F7V star while the secondary is a K1V star (Seach et al. 2020). The orbital period of the binary is ∼280 d (Tomkin et al. 1987) and the system has an estimated age of ∼5 Gyr (Casagrande et al. 2011), making it one of the oldest F stars studied using ZDI. The longitudinal magnetic field strength of the primary has been measured previously by Lee et al. (2018) and Seach et al. (2020) with the results from Lee et al. (2018) showing the longitudinal magnetic field varying from ∼−11 to +11 G with a period of ∼23.4 d. This has been interpreted as the rotational period of the primary, and the positive to negative changes in the longitudinal magnetic field would seem to indicate that the star has a moderately strong magnetic field that is more complex than a simple dipolar field aligned with the stellar rotation axis.

Expanding upon the work of Lee et al. (2018), we have observed χ Dra spectropolimetrically at four epochs as part of the BRITEpol program (Neiner et al. 2017). From these observations, we improve the orbital parameters of the system (Section 3), measure the chromospheric emission (Section 4) and the longitudinal magnetic field (Section 5) of the star, create magnetic maps at each epoch to look for a potential rapid cycle as seen on other late-F stars (Section 6) and look for evidence of the high levels of differential rotation commonly seen on late-F stars (Section 7). In Section 8, we use the magnetic maps created to model the stellar wind from χ Dra A at the four epochs.

2 OBSERVATIONS AND DATA REDUCTION

χ Dra (HD 170153, HIP 89937, HR 6927) was originally observed as part of the BRITEpol project (Neiner et al. 2017) which, as support for the BRITE (BRIght-star Target Explorer) satellite campaign (Weiss et al. 2014), observed every star brighter than $V = 4$ in circularly polarized light to look for stellar magnetic fields. The primary of χ Dra (F7V) was shown to host a magnetic field with a longitudinal magnetic field strength of $B_l = -6.3 \pm 1.2$ G (Seach et al. 2020), in agreement with the earlier observations of Lee et al. (2018), and thus was chosen for follow-up studies in order to map the magnetic field topology. The stellar parameters for χ Dra A used/found in this study are given in Table 1.

2.1 Observations

χ Dra was observed over four epochs using the 2-m Téléscope Bernard Lyot (TBL) at Pic du Midi, in France. Observations were obtained in 2014 May–August, 2015 March–June, 2016 August,

Table 2. Observation log for the 2014 and 2015 epochs. Column 1 gives the UT date of the observation and column 2 gives the polarization state observed. Column 3 gives the mid-HJD of the observations, while columns 4 and 5 give the radial velocity measurement of the primary and secondary, respectively. Column 6 gives the orbital phase of the observation, based on our improved orbital parameters (see Section 3) and column 7 gives the S-index measured from each observation (see Section 4). Typical uncertainties for NARVAL radial velocities are 30 m s^{-1} (Petit et al. 2021).

UT date	Pol.	Mid-HJD ($-2,450,000$)	RV pri (km s^{-1})	RV sec (km s^{-1})	Orb. phase	S-index
2014						
May 5	V	6783.50017	33.06	–	0.41787	0.172
Jul 14	V	6853.43743	43.34	17.2	0.66711	0.173
Jul 16	V	6855.41466	43.56	16.9	0.67416	0.174
Jul 17	V	6856.50808	43.67	16.7	0.67805	0.173
Aug 11	V	6881.33882	45.84	13.6	0.76655	0.174
Aug 20	V	6890.49443	46.15	13.2	0.79917	0.177
2015						
Mar 9	V	7091.73841	37.69	25.5	0.51637	0.178
Mar 11	V	7093.71244	37.96	25.2	0.52340	0.177
Mar 12	V	7094.70057	38.10	25.0	0.52692	0.179
Mar 16	V	7098.68244	38.63	23.7	0.54111	0.179
Apr 1	V	7114.68464	40.92	20.8	0.59814	0.176
Apr 13	V	7126.48671	42.38	18.5	0.64020	0.175
Apr 14	V	7127.55129	42.53	18.3	0.64400	0.186
Apr 23	V	7136.58240	43.52	16.7	0.67618	0.173
Apr 29	V	7142.56701	44.17	15.8	0.69751	0.176
May 11	V	7154.64626	45.26	14.2	0.74056	0.173
May 16	V	7159.63260	45.59	13.7	0.75833	0.172
May 17	V	7160.65208	45.64	13.6	0.76196	0.173
May 27	V	7170.42396	46.07	13.2	0.79679	0.173
May 28	V	7171.46764	46.10	13.2	0.80050	0.175
May 30	V	7173.39977	46.07	13.1	0.80739	0.173
Jun 1	V	7175.51723	46.11	13.2	0.81494	0.173

and 2019 June–July. All observations were taken with the NARVAL spectropolarimeter (Aurière 2003) with the vast majority being taken in circularly polarized light, Stokes *V*, although in 2016 several observations were taken using linear polarization, Stokes *Q* and *U* (see Tables 2, 3, and 4). We used the linear polarization measurements to determine the radial velocity (Section 3) and measure the Ca II H&K emission (Section 4). However, the magnetic mapping program used to create the magnetic field maps (ZDIPY, see Section 6) is not designed to incorporate Stokes *Q* and *U* observations, so these were not included in the creation of the magnetic field maps. No magnetic field was detected in any of the Stokes *Q* or *U* observations.

NARVAL is a bench mounted Èchelle spectropolarimeter with a spectral wavelength coverage in a single exposure from 370 to 1050 nm with small gaps at 922.4–923.4, 960.8–963.6, and 1002.6–1007.4 nm. When in spectropolarimetric mode, NARVAL has a resolving power of ~68 000. Each Stokes *V*, *Q*, or *U* observation is calculated from a series of four Stokes *I* (Intensity) sub-exposures, with each sub-exposure measuring the intensity in the two orthogonal polarization states. The polarization state is switched between sub-exposures to minimize any instrumental effects on the polarization signature. The exposure time of each observation was 4 × 120 s for the 2014 and 2015 observations, 4 × 180 s for the 2016 observations (including the Stokes *Q* and *U* observations), and 4 × 100 s for the 2019 observations.

2.2 Data reduction

The NARVAL observations were reduced and calibrated in-house using the LIBRE-ESPRIT software reduction package. LIBRE-ESPRIT

is based on ESPRIT (Échelle spectra reduction: an interactive tool) which is detailed in Donati et al. (1997) and produces normalized wavelength calibrated spectra. For all observations, a Stokes *I* spectrum was created by combining each of the four sub-exposures together for every observation, while a Stokes *V*, *Q*, or *U* spectra was created, for the relevant observations, by separating sub-exposures with orthogonal polarization states. A null spectrum is also created by separating sub-exposures with the same polarization states and acts as a check on the validity of any magnetic signature detected in the Stokes *V*, *Q*, or *U* profile. More details on the data reduction methodology can be found in Donati et al. (1997) or Marsden et al. (2014).

As the polarization signals in individual spectral lines are small, but similar in each line, the technique of least-squares deconvolution (LSD; Donati et al. 1997) is used to enhance the signal by creating an 'average' spectral line from the several thousand in each Échelle spectrum (~7400 lines used). LSD assumes a weak-field regime in the 'addition' of the spectral lines with further information on the LSD technique found in Donati et al. (1997) and Kochukhov, Makaganiuk & Piskunov (2010). To create the LSD profile requires the use of a line mask with similar properties to the star. In this case, we used one of the line masks from the BCool project (Marsden et al. 2014) with an effective temperature of 6000 K, $\log g = 4.5$ cm s^{-2}, and $\log (M/H) = -0.20$. The stellar parameters for χ Dra given by Luck (2017) are $T_{\mathrm{eff}} = 6083$ K, $\log g = 4.2$ cm s^{-2}, and $\log (Fe/H) = -0.64$. Though the metallicity of χ Dra is lower than the value used for the selected mask, previous testing (Marsden et al. 2014) has shown that the metallicity does not have a significant impact on the LSD profile produced. LSD was applied to all the reduced spectra, Stokes *I*, *V*, *Q*, and *U*, and the resultant signal-to-noise ratios (SNRs) for the Stokes *V*, *Q*, or *U* LSD profiles are given in Table 5, with the velocity step of the LSD profiles created to match the pixel size of NARVAL at 1.8 km s^{-1}. For those nights where there are multiple observations (epochs 2016 and 2019), given a rotational period of 23.39 d (Lee et al. 2018) and an orbital period of 280.5 d (see Section 3), we have added the observations taken on a single night together as the phase shift between the observations is minimal.

3 IMPROVED ORBITAL PARAMETERS

An example of one of the LSD profiles for χ Dra is shown in Fig. 1, at a phase where the primary and secondary of the system are well separated. Using the created LSD profiles it is possible to update the orbital ephemeris of χ Dra. As expected for a very bright star the orbital parameters of χ Dra have been previously determined in a number of studies (see Tomkin et al. 1987, Farrington et al. 2010, Torres et al. 2010, Lee et al. 2018, and references therein). Tomkin et al. (1987) measured the radial velocities of both the primary and secondary and found χ Dra A to be a near solar mass star ($M_{\mathrm{P}} = 1.03 \pm 0.03$ M$_{\odot}$), while the secondary had a mass of $M_{\mathrm{S}} = 0.75 \pm 0.02$ M$_{\odot}$. This was found using an orbital inclination of $74.9 \pm 0.9°$, and the system was found to have an eccentricity of $e = 0.445$ with an orbital period of 280.55 d. Lee et al. (2018) further refined the obit of the system based on radial velocity measurements of only the primary. Farrington et al. (2010) looked at the orbit of χ Dra using the long baseline Center for High Angular Resolution Astronomy (CHARA) array (ten Brummelaar et al. 2005). This determined an orbital period of 280.528 ± 0.0228 d and an orbital inclination of $74.42 \pm 0.58°$.

From the LSD profiles we have created it is possible to measure the radial velocity of both the primary and the secondary by fitting a Gaussian profile (the bisector was also tried and gave extremely

Table 3. Same as Table 2, but for the 2016 observations.

UT date	Pol.	Mid-HJD (−2,450,000)	RV pri (km s⁻¹)	RV sec (km s⁻¹)	Orb. phase	S-index
2016						
Aug 10	Q	7611.35223	31.33	–	0.36816	0.175
Aug 10	U	7611.36369	31.34	–	0.36820	0.174
Aug 10	V	7611.37515	31.33	–	0.36825	0.174
Aug 11	V	7612.34819	31.50	–	0.37171	0.175
Aug 11	V	7612.42622	31.52	–	0.37199	0.175
Aug 12	V	7613.35326	31.63	–	0.37529	0.175
Aug 12	V	7613.53782	31.65	–	0.37595	0.175
Aug 13	V	7614.52591	31.80	–	0.37947	0.174
Aug 14	Q	7615.41846	31.92	–	0.38265	0.174
Aug 14	Q	7615.42973	31.92	–	0.38269	0.174
Aug 14	Q	7615.44085	31.92	–	0.38273	0.174
Aug 14	Q	7615.45210	31.93	–	0.38277	0.174
Aug 14	U	7615.46365	31.92	–	0.38282	0.175
Aug 14	U	7615.47476	31.92	–	0.38286	0.174
Aug 14	U	7615.48599	31.93	–	0.38290	0.174
Aug 14	U	7615.49716	31.93	–	0.38294	0.174
Aug 14	V	7615.50875	31.93	–	0.38298	0.174
Aug 18	V	7619.33988	32.40	–	0.39663	0.175
Aug 18	V	7619.44181	32.42	–	0.39699	0.175
Aug 20	V	7621.38238	32.61	–	0.40391	0.175
Aug 20	V	7621.45259	32.63	–	0.40416	0.175
Aug 21	V	7622.34158	32.74	–	0.40733	0.175
Aug 21	V	7622.38705	32.76	–	0.40749	0.174
Aug 22	V	7623.39835	32.87	–	0.41109	0.174
Aug 22	V	7623.46822	32.88	–	0.41134	0.175
Aug 23	V	7624.39779	32.99	–	0.41466	0.174
Aug 23	V	7624.47253	32.99	–	0.41492	0.174
Aug 24	V	7625.39481	33.11	–	0.41821	0.174
Aug 24	V	7625.46434	33.10	–	0.41846	0.174
Aug 29	V	7630.49895	33.81	–	0.43640	0.174
Aug 30	V	7631.33704	33.89	–	0.43939	0.174
Aug 30	V	7631.49824	33.92	–	0.43996	0.174

similar results) to both the primary and secondary profiles, although for the secondary this can only be done when it is separated from the primary. The radial velocities are given in Tables 2, 3, and 4. Comparing radial velocity measurements determined from LSD profiles taken on the same night, the shift between them was of the order of 0.01 km s⁻¹ for the primary and ∼0.1 km s⁻¹ for the secondary. Given that the radial velocity precision for NARVAL is around 0.03 km s⁻¹ (Petit et al. 2021), we have adopted errors of 0.03 and 0.3 km s⁻¹ for the primary and secondary, respectively. However, where the primary and secondary profiles are overlapping the error bar is increased to 0.5 and 1.0 km s⁻¹ for the primary and secondary, respectively.

We have combined our new radial velocity measurements with those of Tomkin et al. (1987) and Lee et al. (2018). For the Lee et al. (2018) measurements, we have used the published 1σ values for the error bars. However, for the Tomkin et al. (1987) measurements no error bar is provided. Based on the residuals for our fits, we have estimated error bars of 2 and 3 km s⁻¹ for the primary and secondary, respectively.

We have then used the RVFIT orbital fitting routine of Iglesias-Marzoa, López-Morales & Morales (2015) to determine new orbital parameters for the system. The fits are given in Fig. 2 with the determined parameters given in Table 6. We also checked our orbital fit using the fitting routine ELISA (Čokina, Fedurco & Parimucha 2021), which gave values consistent with the results shown in Table 6. Using the orbital inclination of the system of

74.42 ± 0.58° from Farrington et al. (2010), we get a primary mass of $M_P = 1.00 \pm 0.01$ M$_\odot$ and a secondary mass of $M_S = 0.71 \pm 0.01$ M$_\odot$, slightly lower than that of Tomkin et al. (1987). An orbital eccentricity of $e = 0.422975 \pm 0.000143$ and an orbital period of $P = 280.611713 \pm 0.000043$ d are also found. As has been noted by Tomkin et al. (1987), the primary's mass is rather low for an F7V star, with an estimated radius of 1.2 R$_\odot$ (Torres et al. 2010).

4 CA II H&K EMISSION

The emission cores of the Ca II H and K lines at 3968.492 and 3933.682 Å, respectively, have long been used as a measure of the magnetic activity of a star. The most commonly used measure of the Ca II H&K emission is the S-index introduced by Wilson (1978) as part of the Mount Wilson chromospheric activity survey of solar-type stars. For stars observed outside of the Mount Wilson survey, observations can be converted to the S-index by

$$\text{S-index} = \frac{aF_H + bF_K}{cF_R + dF_V} + e, \qquad (1)$$

where F_H and F_K are the fluxes in the HK lines from 1 Å-wide triangular bandpasses centred on the lines at 3968.492 and 3933.682 Å, respectively. While F_R and F_V are two 20 Å-wide channels centred on 4001.07 and 3901.07 Å (Wright et al. 2004). The five coefficients (a, b, c, d, e) allow calibration from a given telescope

Table 4. Same as Table 2, but for the 2019 observations.

UT date	Pol.	Mid-HJD (−2,450,000)	RV pri (km s⁻¹)	RV sec (km s⁻¹)	Orb. phase	S-index
2019						
Jun 15	V	8650.39191	11.53	61.8	0.07109	0.180
Jun 15	V	8650.40117	11.54	61.8	0.07112	0.181
Jun 15	V	8650.41050	11.54	61.8	0.07115	0.181
Jun 15	V	8650.41983	11.54	61.8	0.07119	0.180
Jun 16	V	8651.42313	11.59	61.7	0.07476	0.179
Jun 16	V	8651.43244	11.61	61.7	0.07480	0.179
Jun 16	V	8651.44179	11.61	61.8	0.07483	0.180
Jun 16	V	8651.45115	11.62	61.8	0.07486	0.179
Jun 18	V	8653.42771	11.81	61.5	0.08191	0.181
Jun 18	V	8653.43718	11.81	61.5	0.08194	0.182
Jun 18	V	8653.44682	11.81	61.5	0.08197	0.181
Jun 18	V	8653.45697	11.80	61.5	0.08201	0.182
Jun 21	V	8656.44147	12.27	60.9	0.09265	0.180
Jun 21	V	8656.45096	12.27	60.9	0.09268	0.181
Jun 21	V	8656.46040	12.28	60.9	0.09271	0.180
Jun 21	V	8656.46983	12.27	60.9	0.09275	0.181
Jun 22	V	8657.37039	12.47	60.7	0.09596	0.180
Jun 22	V	8657.37971	12.47	60.7	0.09599	0.179
Jun 22	V	8657.38906	12.47	60.7	0.09602	0.180
Jun 22	V	8657.39825	12.48	60.7	0.09606	0.178
Jun 30	V	8665.40447	14.34	58.0	0.12459	0.178
Jun 30	V	8665.41385	14.34	58.0	0.12462	0.178
Jun 30	V	8665.42329	14.33	58.0	0.12466	0.178
Jun 30	V	8665.43276	14.34	58.0	0.12469	0.178
Jul 11	V	8675.56422	17.12	54.0	0.16080	0.179
Jul 11	V	8675.57371	17.12	54.0	0.16083	0.180
Jul 11	V	8675.58294	17.13	54.0	0.16086	0.179
Jul 11	V	8675.59229	17.13	54.0	0.16090	0.179
Jul 16	V	8681.40335	18.76	51.7	0.18161	0.179
Jul 16	V	8681.41274	18.75	51.7	0.18164	0.191
Jul 16	V	8681.42227	18.77	51.7	0.18167	0.176
Jul 16	V	8681.43177	18.77	51.7	0.18171	0.179
Jul 18	V	8683.39947	19.33	50.9	0.18872	0.180
Jul 18	V	8683.40887	19.33	50.9	0.18875	0.179
Jul 18	V	8683.41834	19.34	50.9	0.18879	0.179
Jul 18	V	8683.42785	19.34	50.9	0.18882	0.180
Jul 19	V	8684.39994	19.62	50.5	0.19229	0.180
Jul 19	V	8684.40937	19.62	50.5	0.19232	0.180
Jul 19	V	8684.41895	19.63	50.5	0.19235	0.180
Jul 19	V	8684.42859	19.63	50.5	0.19239	0.182
Jul 20	V	8685.43126	19.89	50.1	0.19596	0.180
Jul 20	V	8685.44250	19.89	50.1	0.19600	0.180
Jul 20	V	8685.45204	19.90	50.1	0.19603	0.180
Jul 20	V	8685.46153	19.90	50.1	0.19607	0.180
Jul 23	V	8688.39495	20.70	49.0	0.20652	0.179
Jul 23	V	8688.40441	20.70	49.0	0.20656	0.179
Jul 23	V	8688.41393	20.70	49.0	0.20659	0.178
Jul 23	V	8688.42339	20.71	49.0	0.20662	0.178

system to the Mount Wilson S-index. For our measurements, we have used the NARVAL coefficients determined by Marsden et al. (2014).

The S-index for each measurement is given in Tables 2, 3, and 4, and values range from 0.172 to 0.191 with a mean of 0.177. This is similar to the value of 0.175 ± 0.002 given in Seach et al. (2020), unsurprisingly as they used one of the observations presented here, but slightly higher than previous values which range from 0.152 to 0.161 (Pace 2013). A generalized Lomb–Scargle analysis (Zechmeister & Kürster 2009) of the data to look for periods did not find any (see Fig. A1), however, a very slight increase in the S-index

for the 2019 observations is seen compared to the 2014, 2015, and 2016 observations, see Table 7. The values are plotted in Fig. 3.

5 LONGITUDINAL MAGNETIC FIELD

The magnetic field over the visible surface of a star can be estimated from a single Stokes I and V LSD profile using the formula from Donati et al. (1997):

$$B_l = -2.14 \times 10^{11} \frac{\int v V(v) dv}{\lambda g c \int [I_c - I(v)] dv}, \tag{2}$$

Table 5. Summary of the Stokes *V* LSD observations for χ Dra. Column 1 gives the UT date and column 2 gives the mid-HJD of the observations. Column 3 gives the SNR of the Stokes *V* LSD profiles. Column 4 gives the longitudinal magnetic field measurements from the LSD profiles, while column 5 gives the longitudinal magnetic field measurement from the null observations (should be zero, see Section 5).

| UT date	Mid-HJD $(-2,450,000)$	LSD SNR	B_l (G)	N_l (G)
2014				
May 5	6783.50017	27 895	-3.7 ± 0.8	0.0 ± 0.8
Jul 14	6853.43743	28 212	-2.9 ± 0.9	1.3 ± 0.9
Jul 16	6855.41466	35 705	-4.5 ± 0.7	1.2 ± 0.7
Jul 17	6856.50808	29 258	-4.9 ± 0.9	0.8 ± 0.9
Aug 11	6881.33882	32 873	-4.5 ± 0.8	0.4 ± 0.8
Aug 20	6890.49443	33 958	-4.1 ± 0.8	0.6 ± 0.8
2015				
Mar 9	7091.73841	36 086	-5.5 ± 0.7	0.2 ± 0.7
Mar 11	7093.71244	34 344	-4.7 ± 0.7	0.7 ± 0.8
Mar 12	7094.70057	34 033	-3.0 ± 0.8	-0.1 ± 0.8
Mar 16	7098.68244	32 602	-4.0 ± 0.8	0.9 ± 0.8
Apr 1	7114.68464	39 532	-3.2 ± 0.7	-0.3 ± 0.7
Apr 13	7126.48671	36 745	-3.9 ± 0.7	-1.2 ± 0.7
Apr 14	7127.55129	29 826	-4.3 ± 0.9	-0.1 ± 0.9
Apr 23	7136.58240	36 991	-3.3 ± 0.7	0.1 ± 0.7
Apr 29	7142.56701	38 678	-3.1 ± 0.7	-1.3 ± 0.7
May 11	7154.64626	27 188	-5.0 ± 1.0	-0.5 ± 1.0
May 16	7159.63260	45 174	-3.6 ± 0.6	-0.2 ± 0.6
May 17	7160.65208	35 774	-3.6 ± 0.8	-0.1 ± 0.8
May 27	7170.42396	37 852	-3.9 ± 0.7	-0.3 ± 0.7
May 28	7171.46764	31 955	-4.0 ± 0.8	-0.3 ± 0.8
May 30	7173.39977	38 606	-3.0 ± 0.7	-0.3 ± 0.7
Jun 1	7175.51723	35 013	-3.2 ± 0.8	0.5 ± 0.8
2016				
Aug 10	7611.37515	49 666	-3.9 ± 0.5	0.5 ± 0.5
Aug 11	7612.38720	62 345	-3.4 ± 0.4	-0.3 ± 0.4
Aug 12	7613.44554	54 551	-2.8 ± 0.4	0.4 ± 0.4
Aug 13	7614.52591	37 248	-2.7 ± 0.6	1.0 ± 0.7
Aug 14	7615.50875	35 537	-1.6 ± 0.7	-0.6 ± 0.7
Aug 18	7619.39085	47 879	-2.4 ± 0.5	0.0 ± 0.5
Aug 20	7621.41749	53 798	-2.3 ± 0.4	0.2 ± 0.4
Aug 21	7622.36431	60 825	-2.2 ± 0.4	0.0 ± 0.4
Aug 22	7623.43328	48 178	-1.4 ± 0.5	-0.6 ± 0.5
Aug 23	7624.43516	57 896	-2.8 ± 0.4	0.4 ± 0.4
Aug 24	7625.42958	61 036	-2.3 ± 0.4	0.5 ± 0.4
Aug 29	7630.49895	39 823	-3.2 ± 0.6	-0.1 ± 0.6
Aug 30	7631.41764	58 575	-2.3 ± 0.4	-0.2 ± 0.4
2019				
Jun 15	8650.40585	62 196	-2.7 ± 0.4	0.2 ± 0.4
Jun 16	8651.43713	42 131	-2.8 ± 0.6	0.0 ± 0.6
Jun 18	8653.44217	38 479	-2.7 ± 0.7	1.0 ± 0.7
Jun 21	8656.45567	54 618	-3.6 ± 0.5	0.1 ± 0.5
Jun 22	8657.38435	28 146	-2.9 ± 0.9	-0.2 ± 0.9
Jun 30	8665.41859	55 567	-3.2 ± 0.5	-0.5 ± 0.5
Jul 11	8675.57829	58 924	-2.0 ± 0.4	0.5 ± 0.4
Jul 16	8681.41753	13 734	-2.5 ± 1.9	1.4 ± 1.9
Jul 18	8683.41363	69 668	-3.1 ± 0.4	-0.1 ± 0.4
Jul 19	8684.41421	54 982	-3.7 ± 0.5	-0.7 ± 0.5
Jul 20	8685.44683	53 256	-4.0 ± 0.5	0.2 ± 0.5
Jul 23	8688.40917	62 500	-3.2 ± 0.4	0.1 ± 0.4
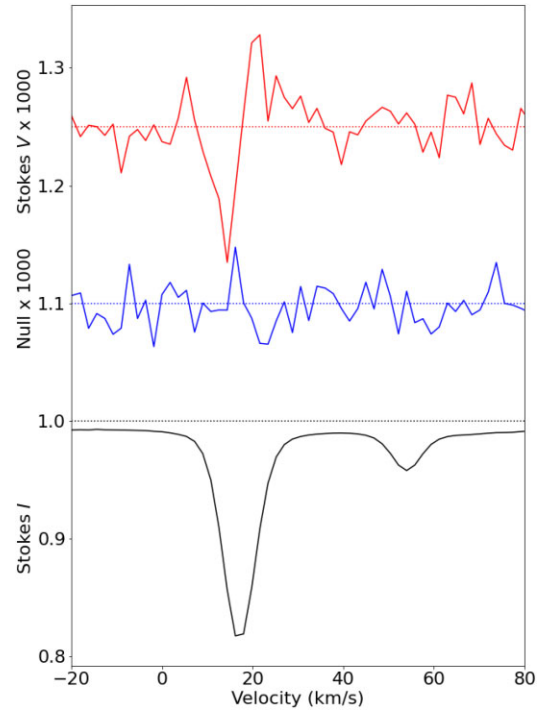
Figure 1. Example of an added Stokes *I* and *V* LSD profile for χ Dra from 2019 July 11 (mid-HJD = 2458675.57829), showing the Stokes *I* profile in black, the Stokes *V* profile in red, and the 'Null' profile in blue. The 'Null' and Stokes *V* profiles have been multiplied by 1000 to highlight the signal and shifted upwards by 1.1 and 1.25, respectively. The Stokes *I* profile shows the primary and the secondary well separated, while the Strokes *V* profile shows a strong magnetic field detection ($B_l = -2.0 \pm 0.4$ G) lining up with the Stokes *I* profile of the primary of the system (deepest Stokes *I* profile), but no detection for the secondary star.

where B_l is the longitudinal magnetic field strength in gauss, *c* is the speed of light, *v* is velocity (as the LSD profiles are created in velocity space), and I_c is the continuum level of the Stokes *I* LSD profile. λ and *g* are the mean wavelength and mean landé factor, respectively, obtained from the LSD profile.

B_l can be calculated from each observation and is an estimate of the magnetic field strength on the visible stellar hemisphere. However, the value obtained can be dependent upon the distribution of magnetic field across the stellar surface, with opposite polarities potentially cancelling out. Thus, B_l is a measure of the large-scale magnetic field on the visible hemisphere.

The value obtained from B_l is dependent not only on the distribution of the surface magnetic field but can depend on the velocity range used in equation (2). If the velocity space used is too wide then noise can be introduced into the calculation impacting the measured magnetic field. Conversely if the velocity space used is too low then signal from the star can be missed. For our observations we have used a velocity range of ± 12 km s^{-1} centred around the velocity of the primary.

There is no evidence of any magnetic field on the secondary of the system in any observations where the secondary is well separated from the primary (see Fig. 1). Therefore, we have assumed that any magnetic field on the secondary (if it exists) is too low to be measured from our observations and thus what we are predominantly measuring is the magnetic field of the primary, even when the Stokes *V* profiles of the two stars are overlapped.
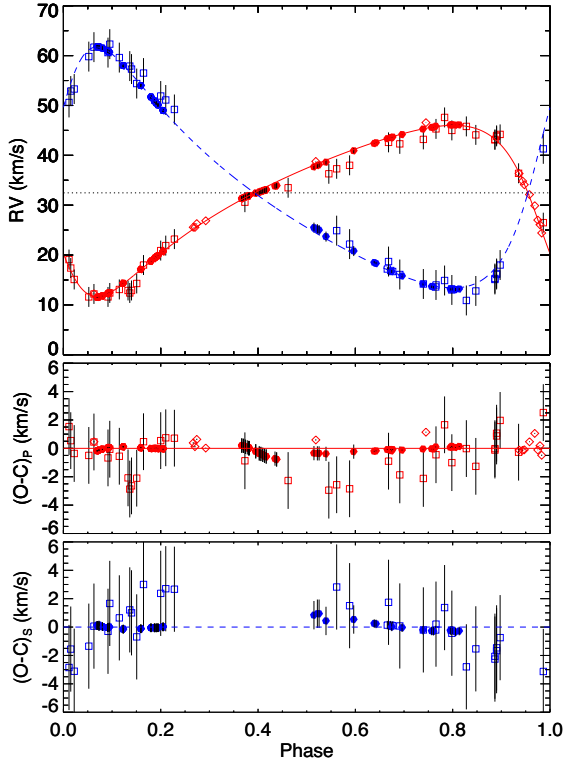
Figure 2. Fit of the χ Dra RV measurements from this study using RVFIT (Iglesias-Marzoa et al. 2015), red being the primary and blue the secondary. The Tomkin et al. (1987) RV measurements (open squares) have no error bars but based on the fit (the O-C values) we have assumed ± 2 km s^{-1} for the primary and ± 3 km s^{-1} for the secondary. For the Lee et al. (2018) values (open diamonds), we are using the published 1σ values as the error bars. For our measurements (solid symbols), measured by finding the centre of a Gaussian fitted to the LSD profile (Section 3), we have assumed the primary error bar is ± 0.03 km s^{-1} and the secondary to be ± 0.3 km s^{-1}. The only exception to this are values near the overlap of the two stars (phases ~ 0.3 to ~ 0.6) where we have taken ± 0.5 km s^{-1} for the primary error and ± 1.0 km s^{-1} for the secondary error. During these phases, the primary and secondary LSD profiles are close together (or overlaid) and thus there is a larger error in the measurement of the centroid of the profiles.

Table 6. χ Dra orbital parameters derived from this study using RVFIT (Iglesias-Marzoa et al. 2015).

Parameter	Value
Adjusted quantities	
P (d)	280.611713 ± 0.000043
T_0 (HJD)	2437304.444247 ± 0.001623
e	0.422975 ± 0.000143
ω (°)	119.923779 ± 0.004922
γ (km s^{-1})	32.474482 ± 0.001346
K_P (km s^{-1})	17.162206 ± 0.005425
K_S (km s^{-1})	24.147726 ± 0.029660
Derived quantities	
$M_P \sin^3 i$ (M$_\odot$)	0.89141618 ± 0.0023945828
$M_S \sin^3 i$ (M$_\odot$)	0.63354488 ± 0.00099080672
$q = M_S/M_P$	0.71071727 ± 0.00090139988
$a_P \sin i$ (10^6 km)	60.007998 ± 0.019476889
$a_S \sin i$ (10^6 km)	84.433009 ± 0.10389313
$a \sin i$ (10^6 km)	144.44101 ± 0.10570304

Table 7. Mean values of the S-index (see Section 4) and longitudinal magnetic field (B_l, see Section 5) for each epoch with the error bars being the standard deviations. Also included is the latitude of the positive pole of the radial dipolar field from the magnetic maps with the given errors being variations as described in Section 6.

Epoch	Mean S-index	Mean B_l (G)	Dipole lat. (°)
2014.53	0.174 ± 0.002	−4.1 ± 0.7	$+83.5^{+1.0}_{-0.0}$
2015.31	0.176 ± 0.004	−3.8 ± 0.7	$+88.5^{+1.0}_{-1.0}$
2016.63	0.174 ± 0.000	−2.6 ± 0.7	$+77.5^{+3.0}_{-6.0}$
2019.51	0.180 ± 0.002	−3.0 ± 0.6	$+80.5^{+1.0}_{-1.0}$
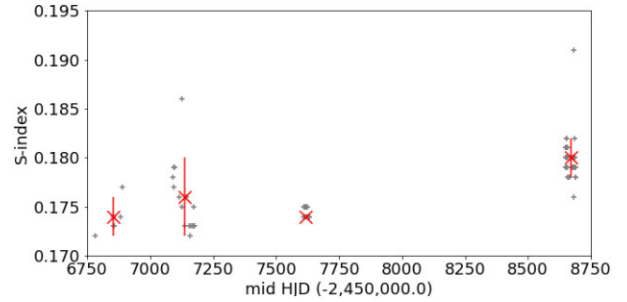
Figure 3. χ Dra S-index measurements. Grey pluses are measurement from the spectra, while the red crosses with error bars show the mean and standard deviation of the measurements for each epoch.
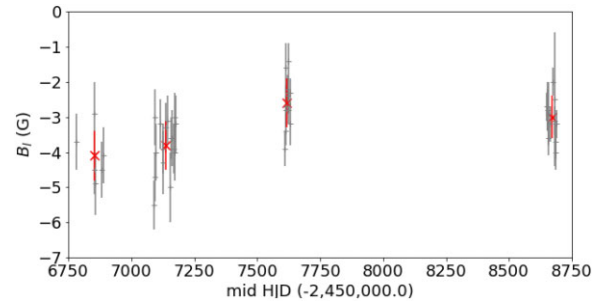

Figure 4. χ Dra B_l magnetic field measurements. Grey pluses are measurement from the spectra, while the red crosses with error bars show the mean and standard deviation of the measurements for each epoch.

The measured B_l for each of our observations is shown in Table 5, where the error was determined by propagation of the uncertainties computed during the reduction process for each spectral bin of the normalized spectrum. We have also applied equation (2) to the 'Null' LSD profile that is created as a check for any systematic errors (see Section 2.2). For the B_l measurement to be considered reliable, the 'Null' measurement should be close to zero (within errors).

As shown in Table 5, all our values of B_l are negative with the mean values for each epoch being similar, within errors (see Table 7). We have plotted the B_l values in Fig. 4. Again a generalized Lomb–Scargle analysis was done (see Fig. A2), but no significant periods were detected.

6 MAGNETIC FIELD MAPS

By observing our target as it rotates, we can invert the Stokes V LSD profiles taken at each rotational phase to reconstruct a surface map of the large-scale magnetic field of the primary of the χ Dra system. To
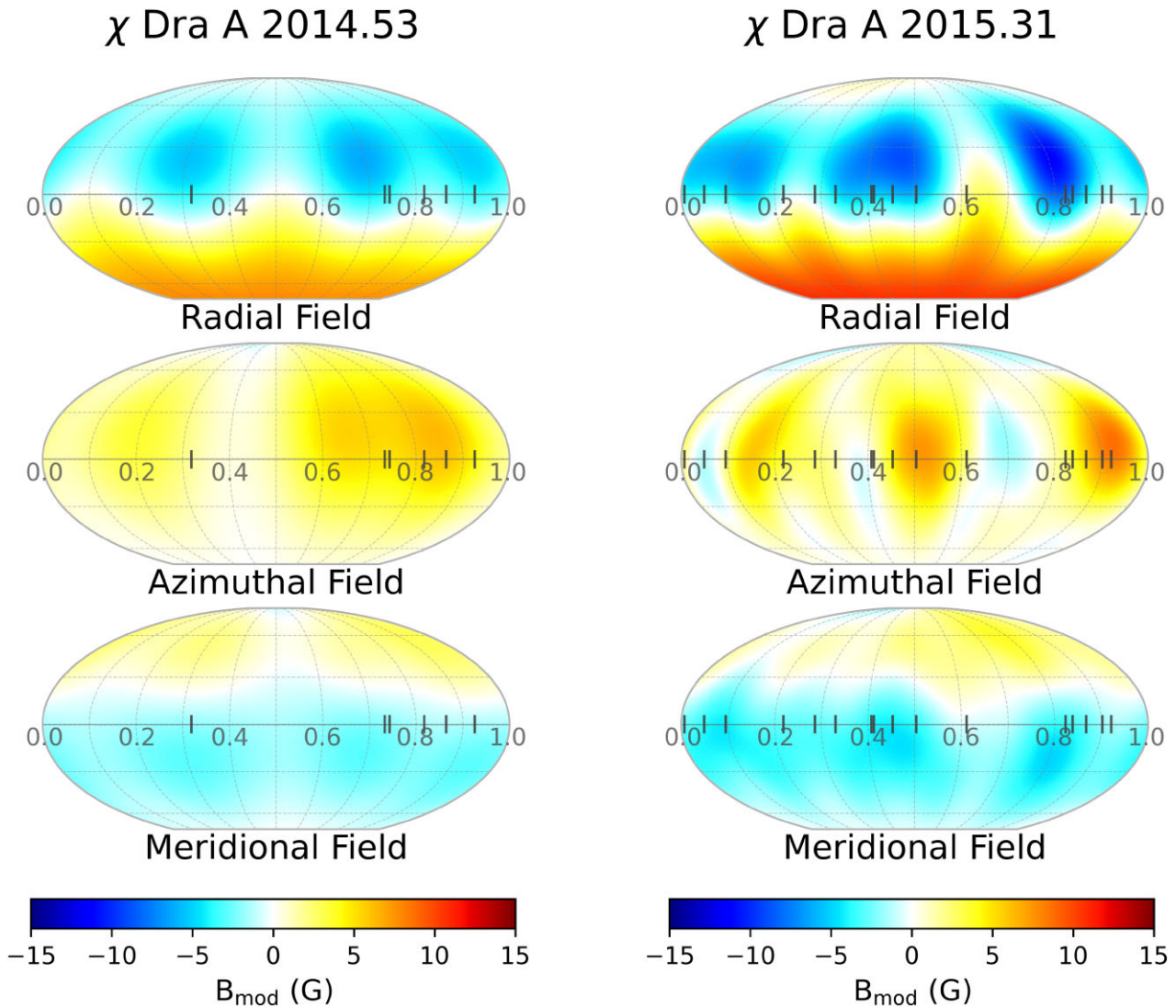
χ Dra A 2014.53

χ Dra A 2015.31

Radial Field

Azimuthal Field

Meridional Field

B_{mod} (G)

Figure 5. Magnetic maps for χ Dra A from 2014 and 2015. The maps are in mollweide projection showing the entire stellar surface down to a latitude of −75°, below which the star is not visible. For each epoch three maps are produced with the top showing the radial magnetic field, the middle the azimuthal, and the bottom the meridional field. Ticks marks at the equator of each map give the phase of the observations while the scale bar at the bottom gives the magnetic field strength in gauss.

reconstruct the magnetic maps of χ Dra A, we have used the ZDIPY inversion code of Folsom et al. (2018) assuming a Voigt profile with solar line parameters (reasonable for a 1.00 M$_\odot$ star) to represent the initial non-rotating LSD profile. The ZDIPY code uses spherical harmonics to express the stellar magnetic field (see Donati et al. 2006, Folsom et al. 2018, and references therein for full details of the use of spherical harmonics and the code). Given that χ Dra A is a slow rotator (v sin i ∼ 2.5 km s^{-1}, Gray 1984), we have limited the maximum spherical harmonic expansion used in the reconstruction to l_{max} = 10 as no change in the maps was seen for any increase beyond this value.

The parameters used in the magnetic field map reconstructions were v sin i = 2.5 km s^{-1} (Gray 1984), a rotational period of P = 23.39 d (Lee et al. 2018) (see Section 7), while the stellar rotational inclination was assumed to be the same as the orbital inclination of 74.42° (Farrington et al. 2010). The radial velocity of the primary (see Tables 2, 3, and 4) was subtracted from each Stokes V LSD profile to remove the motion of the primary star.

As mentioned previously, in order to increase the SNR of the LSD profiles used in the creation of the magnetic maps we have added together those profiles that have been taken on the same night. Given a rotational period of 23.39 d, the maximum separation between observations of ∼4.5 h (on 2016 August 12) equates to a maximum phase shift of less than 1 per cent of the rotational period, so rotational blurring of the features during the combined exposures has virtually no impact on the reconstruction of the magnetic maps.

All the created maps are set to the same starting phase, $T_{phase=0}$ = JD = 2454006.095 to match that from Lee et al. (2018). This JD corresponds to 14:16:48 UT on 2006 September 27, and is a significant amount of time earlier than our data (2014–2019). Given the ± 0.09 d error bar in the rotational period from Lee et al. (2018) (although this may be significantly larger, see Section 7) and the time-base of ∼5 yr for our observations, the error in the phase over our entire map set is likely to be at least ∼30 per cent of the entire rotational phase, so any comparison using phasing between our maps should be taken with caution.
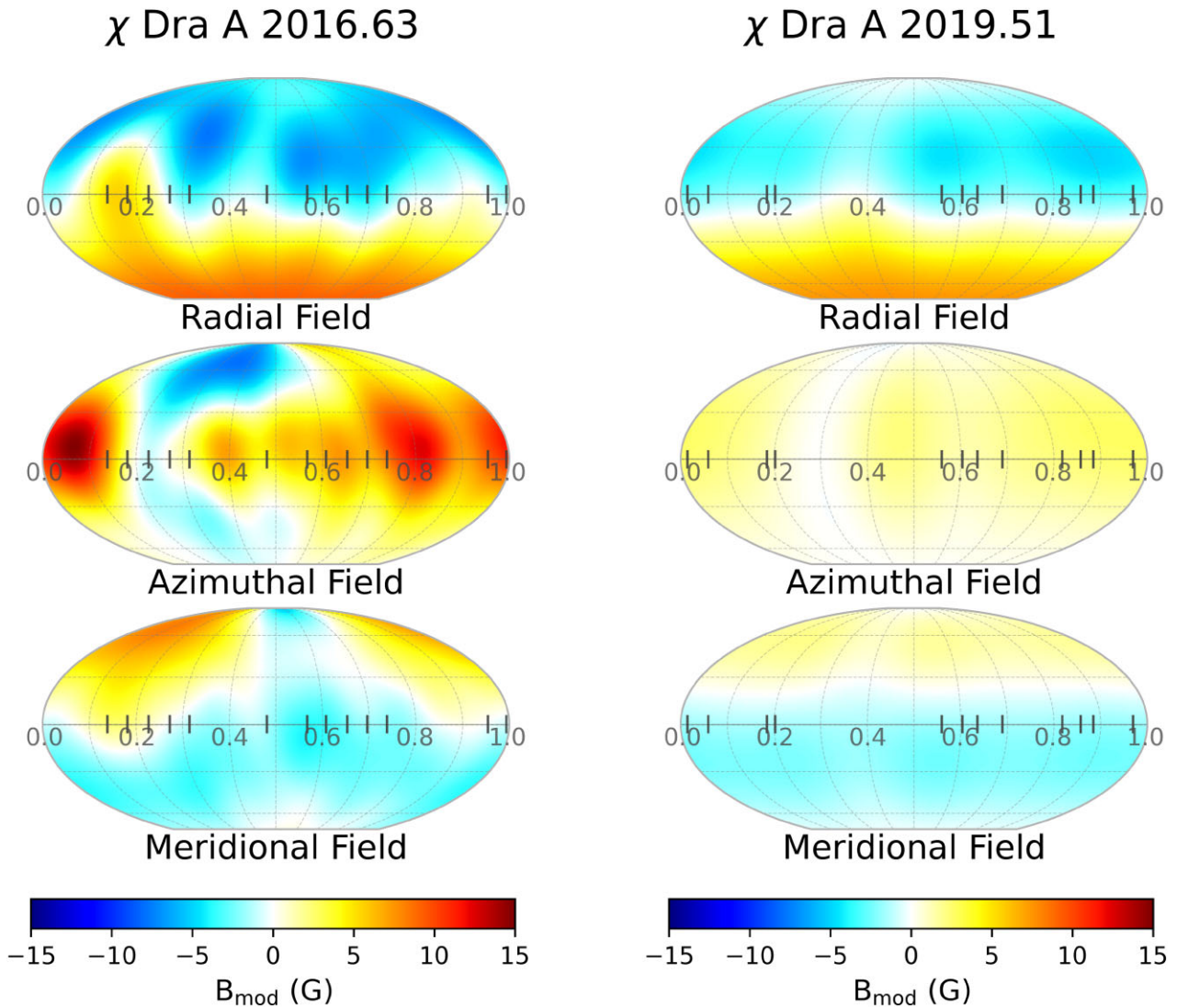
χ Dra A 2016.63

χ Dra A 2019.51

Figure 6. As Fig. 5, but for 2016 and 2019.

The ZDIPY code reconstructs the magnetic field in radial (field lines in/out of the stellar surface), azimuthal (field lines wrapped around the star's rotation axis), and meridional (field lines wrapped around the star from pole to pole) components. The maps from the four epochs were created using a target reduced χ^2_{aim} value of 0.95 and are shown in Figs 5 and 6, while the fits to the observed Stokes *V* LSD profiles are given in Fig. 7. All the maps were created assuming solid-body rotation on the stellar surface (see Section 7).

Given the very low $v \sin i$ value for χ Dra A, it was not possible to reconstruct the brightness features on the stellar surface using Doppler imaging, which typically needs $v \sin i$ values of approximately 20 km s^{-1} (Rice 2002). However, given the very flat light curve of χ Dra obtained from the Transiting Exoplanet Survey Satellite (*TESS*; Ricker et al. 2014) shown in Fig. 8, we can infer that any spot features on χ Dra are significantly smaller than that seen on the typical younger, more active targets used to create brightness maps using Doppler imaging, (e.g. HD 171488, Marsden et al. 2014, and HD 29615, Waite et al. 2015).

As the magnetic maps in Figs 5 and 6 are reconstructed using spherical harmonics it is possible to use these spherical harmonics to determine the components of the reconstructed magnetic field

topologies. These are given in Table 8 for the four epochs of observations, and a plot of selected magnetic parameters versus time is given in Fig. 9. The error bars given in the table are 'variation' bars in that they were determined by varying the stellar parameters (rotational inclination, $v \sin i$, and rotational period) by their respective errors, individually as well as simultaneously. For the stellar inclination, we have used the error in the orbital inclination from Farrington et al. (2010) of $\pm 0.58°$ and for the rotational period we have used the error of ± 0.09 d given by Lee et al. (2018). For the $v \sin i$, we have used the error given by Gray (1984) of ± 0.4 km s^{-1}. A value of $v \sin i = 2.5 \pm 0.4$ km s^{-1} covers the $v \sin i$ values obtained by this work and that of Lee et al. (2018) (see Section 7). Of these parameters, the $v \sin i$ is the most significant contribution to the 'variation' bars found in Table 8.

From the spherical harmonics, the position of the radial dipolar axis can also be determined. Any changes in the position of the positive (or negative) dipole can indicate evolution that could be attributable to a magnetic cycle. For our observations of χ Dra A, the positive radial dipole is located at latitude of $\sim +78°$ to $+89°$ (see Table 7). The longitude of the radial dipole varies more dramatically as the magnetic pole 'bounces' around near the rotational pole.
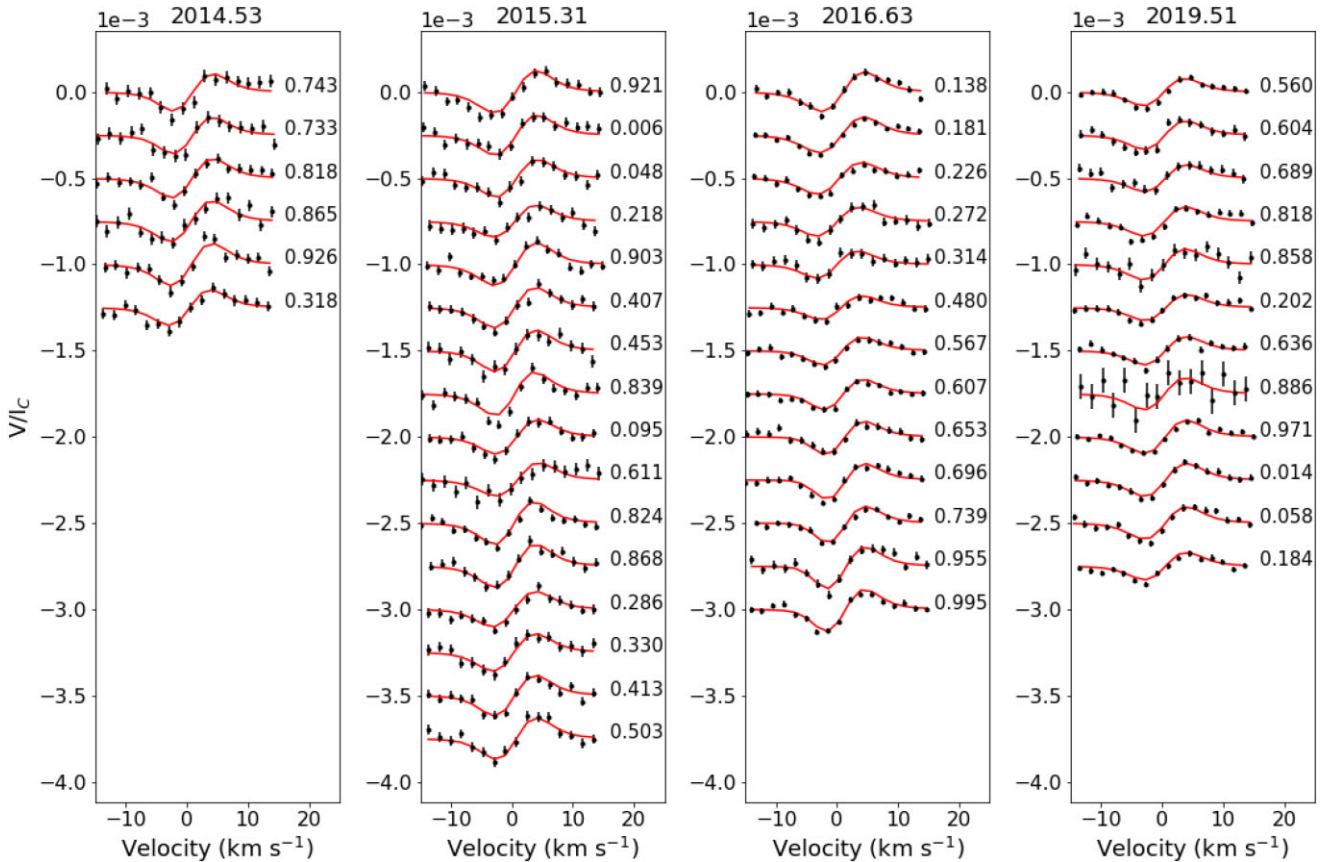
Figure 7. Plot of the Stokes *V* fits (red lines) to the observed Stokes *V* LSD profiles (black data points with errorbars). Each profile is shifted downwards for clarity and the rotational phase of the observation is given next to each profile.
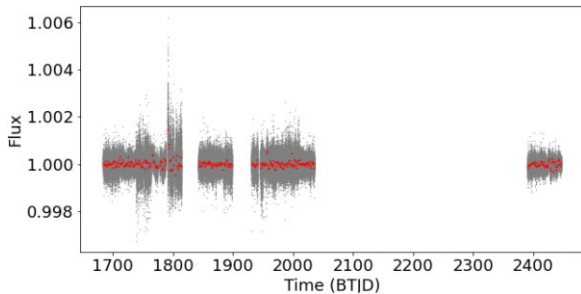

Figure 8. χ Dra *TESS* photometry. Grey dots are SPOC short cadence light curves. The red dots are a re-binning into 1-d periods using a weighted average (1/err).

7 PERIOD SEARCH AND DIFFERENTIAL ROTATION

Lee et al. (2018) determined a rotation period of 23.39 ± 0.09 d for χ Dra A using the measurement of the star's longitudinal magnetic field which varied from approximately -11 G to $+11$ G. In contrast, our longitudinal magnetic field measurements (Section 5) were all found to be negative and no rotational period could be determined from the values. Also as mentioned in Section 4, no period was able to be determined based on modulation of the chromospheric activity of the star either.

χ Dra is part of the Asteroseismic Target list for solar-like oscillations observed in 2-min cadence with *TESS* (Schofield et al.

2019). The short-cadence reduced light curve from the *TESS* Science Processing Operations Center (SPOC; Jenkins et al. 2016) of χ Dra is shown in Fig. 8. As can be seen, the light curve is very flat with little deviations to indicate any indications of large surface spot features. Again a generalized Lomb–Scargle period search was applied to this data (see Fig. A3) and no period could be determined.

As part of the magnetic mapping process (Section 6), a solar-like differential rotation law can be incorporated into the mapping to account for the motion of surface features due to differential rotation during the time-base of the observations. The generalized law used is

$$\Omega(l) = \Omega_{\mathrm{eq}} - d\Omega \sin^2(l), \tag{3}$$

where $\Omega(l)$ is the rotation rate at stellar latitude l, Ω_{eq} is the angular rotation frequency at the equator (converted to rotational period, P_{eq}, for our plots), and $d\Omega$ is the rotational shear between the equator and the poles (the differential rotation). Ω_{eq} and $d\Omega$ are varied for a given entropy value and for each paring a map is created and the reduced χ^2 value is determined. A lower χ^2 value represents a better fit to the observed data for a given pairing of Ω_{eq} and $d\Omega$. This is similar to the process described in Petit, Donati & Collier Cameron (2002) and is described in more detail in Folsom et al. (2018). The resultant χ^2 landscapes for the four epochs of observations are shown in Fig. 10.

As can be seen in Fig. 10, there is no evidence of differential rotation on the surface of χ Dra A, with all epochs showing the lowest χ^2 values around a $d\Omega$ value of zero, indicating that the star is rotating as a solid body.

Table 8. Magnetic parameters of the magnetic maps from Figs 5 and 6. The map epoch is given in the first column while the second and third columns give the mean and maximum magnetic field found on the stellar surface. The fourth and fifth columns give the percentages of the magnetic field energy found in the poloidal and toroidal components of the magnetic field. Columns 6–8, give the per cent of the poloidal magnetic energy found in dipolar ($l = 1$), quadrupolar ($l = 2$), and octopolar ($l = 3$) components, while columns 9–11 give the per cent of the toroidal magnetic energy found in the $l = 1$ to 3 components. Columns 12–14 give the axisymmetry percentage of the total, poloidal, and toroidal magnetic field, respectively. Column 15 gives the strength of the dipolar magnetic field of the star. The errors given in the table are 'variation' bars found from varying the stellar parameters as discussed in Section 6.

| Map	$\|B_{mean}\|$ (G)	$\|B_{max}\|$ (G)	Pol (tot) (per cent)	Tor (tot) (per cent)	Dip (pol) (per cent)	Quad (pol) (per cent)	Oct (pol) (per cent)	Dip (tor) (per cent)	Quad (tor) (per cent)	Oct (tor) (per cent)	Axis (tot) (per cent)	Axis (pol) (per cent)	Axis (tor) (per cent)	Dip (G)
2014.53	$4.8^{+0.3}_{-0.2}$	$8.3^{+0.6}_{-0.3}$	74^{+3}_{-4}	26^{+4}_{-3}	65^{+2}_{-2}	28^{+2}_{-2}	6^{+1}_{-0}	92^{+0}_{-1}	8^{+0}_{-1}	1^{+0}_{-0}	88^{+0}_{-1}	85^{+0}_{-0}	96^{+0}_{-0}	$5.9^{+0.2}_{-0.2}$
2015.31	$6.2^{+1.0}_{-0.1}$	$11.4^{+3.8}_{-0.2}$	86^{+3}_{-2}	14^{+2}_{-3}	54^{+12}_{-22}	29^{+6}_{-4}	13^{+8}_{-6}	73^{+8}_{-14}	6^{+3}_{-1}	12^{+3}_{-4}	82^{+9}_{-17}	82^{+9}_{-17}	76^{+9}_{-16}	$7.5^{+1.0}_{-2.0}$
2016.63	$7.5^{+2.1}_{-0.8}$	$15.0^{+10.2}_{-3.9}$	65^{+6}_{-11}	35^{+11}_{-6}	74^{+3}_{-14}	14^{+4}_{-5}	7^{+4}_{-2}	76^{+11}_{-27}	1^{+2}_{-0}	17^{+20}_{-9}	71^{+8}_{-12}	63^{+12}_{-23}	86^{+3}_{-6}	$8.8^{+0.3}_{-0.4}$
2019.51	$4.0^{+0.1}_{-0.1}$	$7.9^{+0.0}_{-0.1}$	90^{+1}_{-3}	10^{+3}_{-1}	69^{+2}_{-2}	27^{+2}_{-2}	4^{+0}_{-0}	92^{+1}_{-0}	7^{+0}_{-0}	1^{+0}_{-0}	95^{+1}_{-0}	95^{+1}_{-0}	97^{+0}_{-0}	$5.6^{+0.1}_{-0.1}$
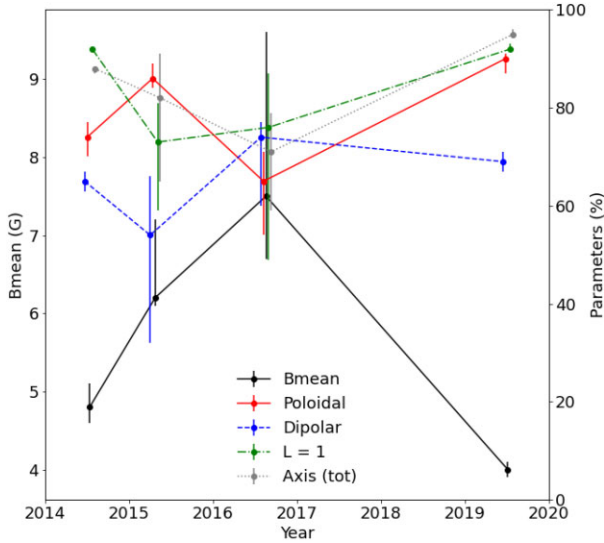
Figure 9. Plot of selected magnetic parameters from Table 8 against the epoch of observation. Plotted are the B_{mean} (black solid line), the percentage of poloidal energy (red solid line), the percentage of the poloidal energy that is dipolar (blue dashed line), the percentage of the toroidal energy in the $l = 1$ component (green dot–dashed line), and the axisymmetry of the total magnetic field (grey dotted line). Each of the data sets are horizontally shifted slightly to more clearly show the 'variation' bars (see Section 6).

A number of potential rotational periods for χ Dra A appear in Fig. 10, with low χ^2 values seen for periods ranging from ~8 to over 30 d. A potential rotational period of ~20–25 d is seen in all epochs, possibly corresponding to the 23.39 d rotational period determined by Lee et al. (2018), but there is no conclusive evidence for a definite rotation period.

As mentioned in Section 6, no brightness map for χ Dra A could be produced. However, we attempted to fit the Stokes I LSD profiles for χ Dra A using ZDIPY and found a best fit to the profiles for a $v\sin i$ value of ~2.2 ± 0.5 km s^{-1}. This was done using the 2019 epoch when the secondary was well separated form the primary. This $v\sin i$ is similar to the value of 2.5 ± 0.4 km s^{-1} from Gray (1984) (which was used in the creation of the magnetic field maps) and the value of ≤ 3 km s^{-1} from Lee et al. (2018).

As was shown by Lee et al. (2018), a rotational period of ~23.4 d is derived using a $v\sin i$ of 2.5 km s^{-1}, a radius of 1.2 R$_\odot$ from Torres et al. (2010) and assuming that the rotational inclination is equal to the orbital inclination of 74.42° from Farrington et al. (2010) (which is probably reasonable for a mature system like χ Dra). Using instead the radius of 1.161 R$_\odot$ from Schofield et al. (2019),

the rotation period is 25.6 d. Both of these values are reasonably close to the 23.39 d period measured by Lee et al. (2018) from the modulation of the B_l and thus, as mentioned in Section 6, we have used a rotational period of 23.39 d and assumed solid-body rotation in the creation of all our magnetic maps. However, in the literature there are a range of $v\sin i$ values for χ Dra, with an number of them being higher than the 2.5 km s^{-1} quoted above. Luck (2017) gives a value of 5.5 km s^{-1}, while Martínez-Arnáiz et al. (2010) give a value of 6.01 km s^{-1}. Both of these values would produce shorter rotational periods for χ Dra A, 10.6 and 9.7 d, respectively, using a radius of 1.2 R$_\odot$ and an inclination angle of 74.42°. Although there appears to be some indication of a possible rotation period around these values in the 2014.53 and 2015.31 epochs (see Fig. 10), there does not appear to be strong evidence for these rotational periods in the 2016.63 and 2019.51 epochs.

8 STELLAR WIND

From the radial field maps in Figs 5 and 6, we created stellar wind models of χ Dra A using the Alfvén wave solar model (AWSoM; Sokolov et al. 2013; van der Holst et al. 2014) which is part of the Space Weather Modelling Framework (SWMF; Tóth et al. 2005, 2012). The model creates three-dimensional maps of the steady-state winds by solving two-temperature magnetohydrodynamic equations, supplemented by two further equations describing the propagation of Alfvén wave energy parallel to the direction of the magnetic field. In AWSoM, the corona is heated by the dissipation of Alfvén wave energy; the flux of Alfvén wave energy across the inner boundary of the model is given by the Pointing flux-to-field ratio (Π_A/B, see Tables 1 and 9), that is, the amount of energy flux is proportional to the local magnetic field strength at the stellar surface. The radial component of the inner surface magnetic field strength in the chromosphere is held at the values in Figs 5 and 6, while the transverse components are free to evolve with the numerical solution.

The transition region and inner corona are modelled using an irregular grid spacing in the radial direction as described by Oran et al. (2013). The AWSoM model extends from the chromosphere to the inner astrosphere at distances ~1 au. We also include heat exchange and cooling terms as they are required to reproduce the slow and fast wind (Roussev et al. 2003). Radiative cooling, given by

$$Q_{rad} = N_i N_e \Lambda (T_e) \tag{4}$$

is included, where N_i and N_e are the ion and electron number densities, respectively, and the rate of cooling curve, $\Lambda(T_e)$, is found using the CHIANTI data base (Landi et al. 2013) by assuming solar composition.
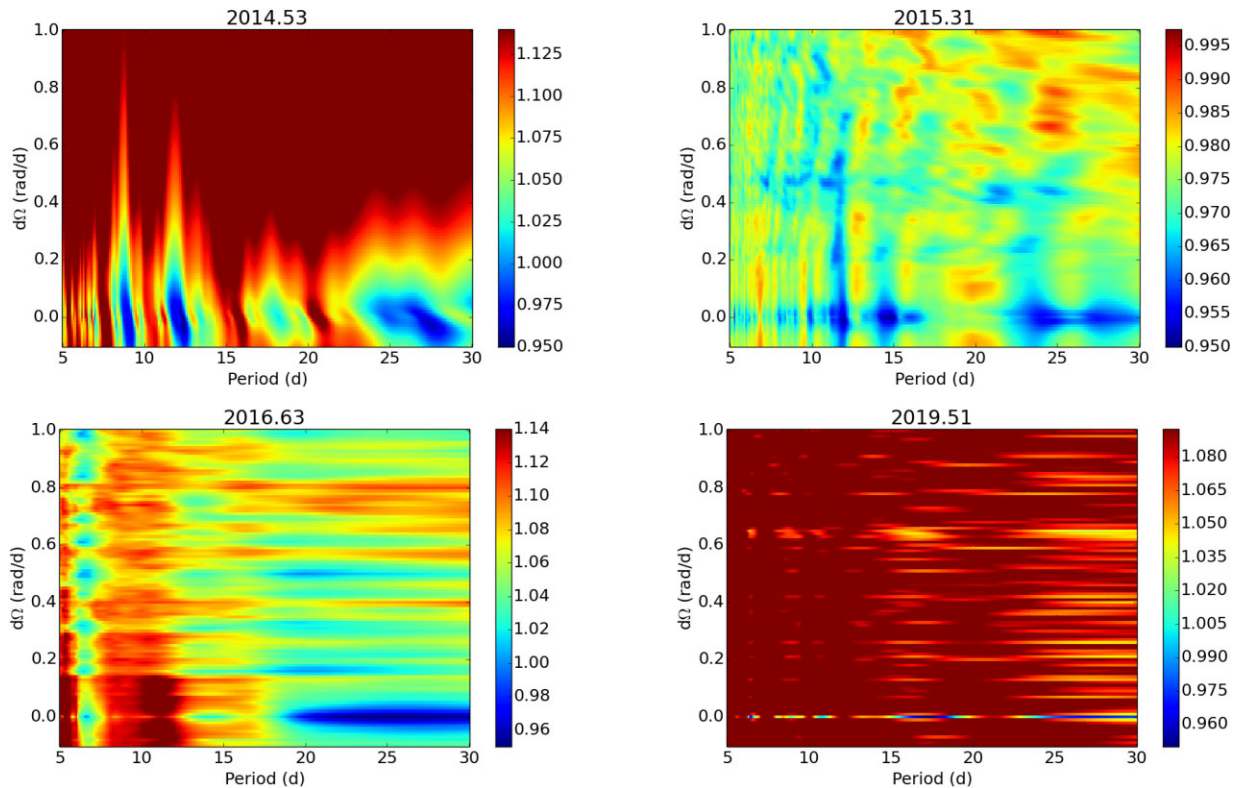
Figure 10. Differential rotation measurements of χ Dra A from the 2014, 2015, 2016, and 2019 data sets. The colourbars show the reduced χ^2 values for each period-differential rotation pairing (P_{eq}, dΩ) with bluer colours representing better fits.

Table 9. Parameters used in the wind modelling of χ Dra A.

Parameter	Value	Reference
Chromospheric base temperature (T_{chr})	5×10^4 K	Alvarado-Gómez et al. (2016a)
Chromospheric base density (n_{chr})	2×10^{17} m^{-3}	Alvarado-Gómez et al. (2016a)
Poynting flux-to-field ratio (Π_A/B)	1.1×10^6 W m^{-2} T^{-1}	Gombosi et al. (2018)
Turbulence transverse correlation length ($L_\perp \sqrt{B}$)	1.5×10^5 mT$^{1/2}$	Gombosi et al. (2018)

As in Seach et al. (2022), solar values are used for the base density and temperature in the chromosphere, for the Poynting flux-to-field ratio, the turbulence transverse correlation length and the Coulomb logarithm as given in Table 9. These values have been shown to accurately reproduce solar conditions (see Sokolov et al. 2013; van der Holst et al. 2014, 2019; Meng et al. 2015; Sachdeva et al. 2019). For a more detailed description of the methodology behind the wind models, see Evensberget et al. (2021, 2022).

8.1 Coronal structure

Fig. 11 shows the magnetic field structure of the final, steady-state wind model solution. The dipolar structure of the magnetic field (Figs 5 and 6) gives rise to polar regions of open field lines separated by an equatorial region where the magnetic field lines are closed. In the 2015 magnetic field maps, a small region surrounding the stellar rotational north pole has positive polarity (see Figs 5 and 6); this can also be seen in the coronal structure of the 2015 panel of Fig. 11. Table 10 gives the average surface radial field strength ($|B_r|$), the wind model average surface field strength ($|B|$), the unsigned magnetic flux over the entire stellar surface (Φ) and the proportion of the unsigned flux (Φ_{open}) associated with open magnetic field lines (truncated lines

in Fig. 11), along with the surface fraction of open magnetic field (S_{open}). The $|B|$ values vary from 4.6 to 6.9 G, while Φ_{open} varies between 0.42 and 0.50 and S_{open} varies between 0.33 and 0.40. The values of S_{open} and Φ_{open} appear to be lower for larger values of $|B|$. When interpreting these values it should be remembered that solar and stellar wind codes often underestimate the open magnetic flux; see the discussion in Linker et al. (2017). In the Alfvén wave solar model, the open magnetic flux can be underestimated by a factor of 2–3 when using solar magnetograms (Sachdeva et al. 2019); this is sometimes corrected for by scaling solar magnetograms by a factor of 1.5–3 (Riley et al. 2021).

8.2 Alfvén surface and current sheet

Fig. 12 shows the Alfvén surface, which is where the local wind speed first exceeds the Alfvén wave speed, given by

$$v_A = \frac{B}{\sqrt{\mu_0 \rho}},\qquad(5)$$

where μ_0 is the permeability of the vacuum and ρ the total mass density of the wind (Alfvén 1942). For all four epochs we observe a two-lobed Alfvén surface which generally corresponds to a dipolar
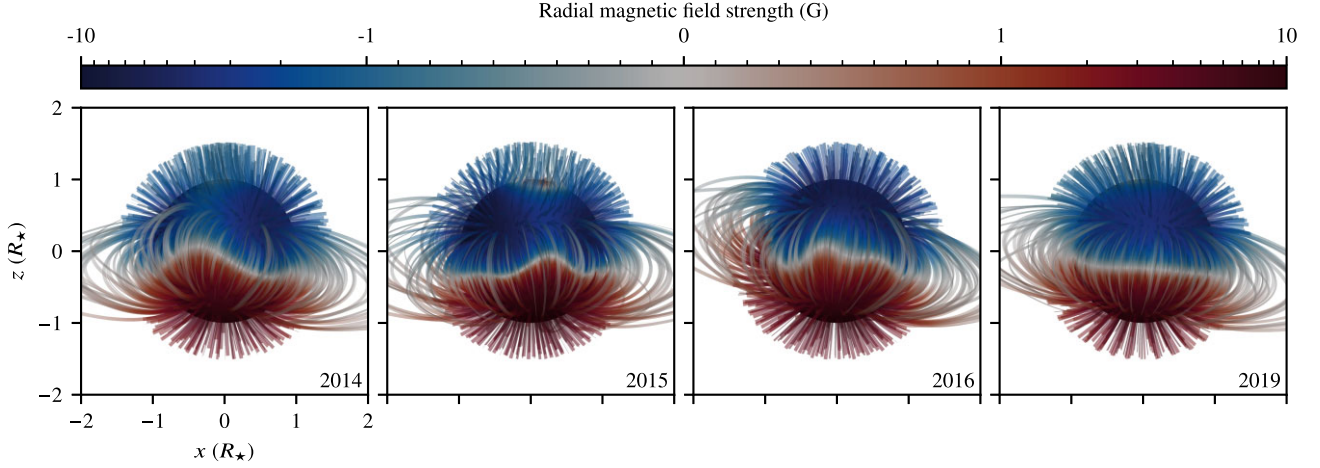
Figure 11. Coronal magnetic field structure of the steady-state wind solution obtained from the radial magnetic field values of Figs 5 and 6. A large number of magnetic field lines are shown to elucidate the magnetic field structure and the distribution of closed and open magnetic field lines. The magnetic field lines are sampled across the surface using a Fibonacci sphere algorithm (Swinbank & Purser 2006). Open magnetic field lines are truncated at $1.5R_\star$. The magnetic field lines and the stellar surface are coloured by the local radial magnetic field strength value. The colour scale is linear between -1 and $+1$ G and logarithmic outside this range, as indicated by the minor tick marks on the colour bar.

Table 10. Key quantities from the wind maps in Figs 11–13. The average surface radial magnetic field strength as found with ZDI is tabulated in the $|B_r|$ column. The total average surface magnetic field strength of the wind solution is given in the $|B|$ column. The Φ column gives the total unsigned surface magnetic flux $\Phi = 4\pi R_\star^2 |B_r|$. The fraction of Φ contained in open magnetic field lines is given in the Φ_{open} column, while the S_{open} column gives the proportion of the surface area containing open field lines. The i_B column gives the magnetic inclination, i.e. the angle between the inner current sheet normal vector and the stellar axis of rotation. Φ_{axi} gives the axisymmetric open flux fraction. R_A and $|r_A \times \hat{\Omega}|$ give the average radial distance to the Alfvén surface and the 'torque-averaged' Alfvén radius, respectively. The $\dot{M}$ and $\dot{J}$ give the steady-state wind mass-loss and wind angular momentum loss rates. The wind pressure for an Earth-like planet is given by $P_w^\oplus$, and the average magnetospheric stand-off distance for an Earth-like planet is given by R_m.

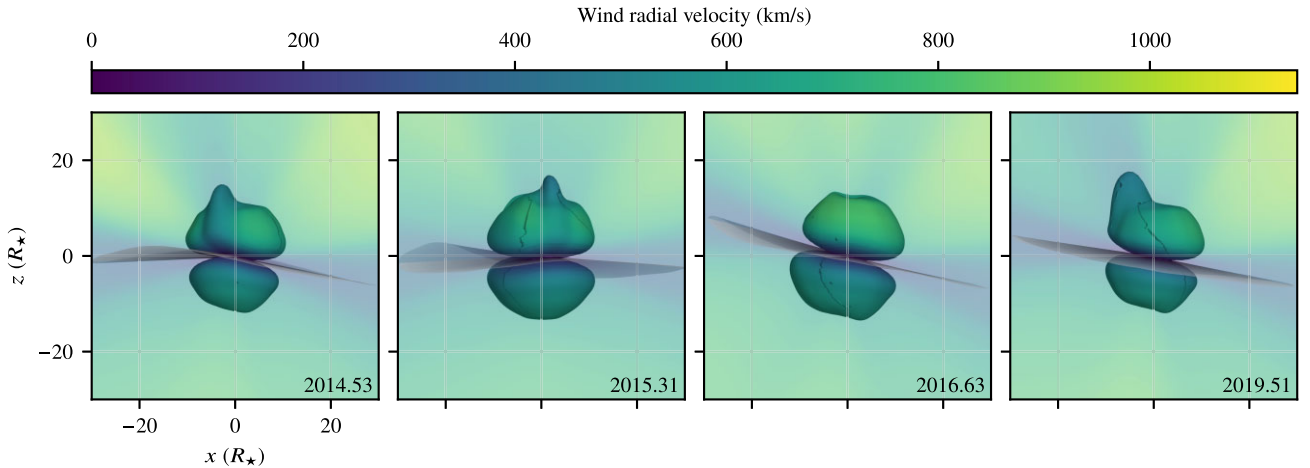| Epoch	$|B_r|$ (G)	$|B|$ (G)	Φ (Wb)	Φ_{open} (Φ)	S_{open} (S)	i_B (°)	Φ_{axi} (Φ_{open})	R_A ($R_\star$)	$|r_A \times \hat{\Omega}|$ ($R_\star$)	$\dot{M}$ (kgs^{-1})	$\dot{J}$ (Nm)	$P_w^\oplus$ (Pa)	R_m (R_p)
2014.53	3.3	4.8	2.9×10^{15}	0.49	0.39	5.9	0.98	10.2	7.7	4.8×10^9	5.6×10^{23}	1.5×10^{-8}	7.1
2015.31	4.6	6.9	4.0×10^{15}	0.42	0.34	1.8	0.99	11.2	8.5	6.2×10^9	8.6×10^{23}	2.1×10^{-8}	6.7
2016.63	4.3	6.2	3.8×10^{15}	0.46	0.33	13.1	0.92	11.3	8.6	5.9×10^9	8.5×10^{23}	1.9×10^{-8}	6.8
2019.51	3.1	4.6	2.8×10^{15}	0.50	0.40	9.2	0.96	10.1	7.6	4.6×10^9	5.4×10^{23}	1.5×10^{-8}	7.1

Figure 12. Alfvén surface, current sheet, and wind radial velocity. The Alfvén surface where the local wind velocity $u = v_A$ is shown as a solid surface; the current sheet where $B_r = 0$ is shown as a translucent grey surface. The Alfvén surface and the plane of sky (xz plane) is coloured by the local radial wind velocity.

coronal magnetic field as seen in Fig. 11. The Alfvén surface and the xz plane are coloured according to the local radial wind speed. The wind speed at the Alfvén surface reaches up to $\sim 0.8 \times 10^6$ m s^{-1}, and wind speeds beyond the Alfvén surface reach up to $\sim 1.1 \times 10^6$ m s^{-1}.

The inner part of the current sheet, where the strength of the radial field is zero, $B_r = 0$ (Schatten 1971), is shown as a grey translucent surface. The magnetic inclination (i_B in Table 10), which is the angle between the stellar axis of rotation (z axis) and the normal vector

of the inner current sheet, varies between $2°$ and $13°$. The average Alfvén radius, R_A, and torque-averaged Alfvén radius, $|r_A \times \hat{\Omega}|$, vary between 10.1 and 11.3 stellar radii and between 7.6 and 8.6 stellar radii, respectively.

The wind mass-loss, $\dot{M}$, and wind angular momentum loss, $\dot{J}$, are also given in Table 10. In the three-dimensional wind maps presented here, $\dot{J}$ and $\dot{M}$ are calculated by integrating over the Alfvén surface, as in Evensberget et al. (2021). This is in contrast to Finley & Matt (2018), where $\dot{J}$ is estimated using the torque-averaged Alfvén radius, and in the one-dimensional models of Weber & Davis (1967) where the Alfvén radius is used in determining $\dot{J}$ ($\dot{J} = \frac{2}{3}\dot{M}\Omega R_A^2$). The wind mass-loss values for χ Dra A are ∼3–6 times higher than the range of solar wind mass-loss values from Mishra et al. (2019), and ∼2 times higher than the wind mass-loss values for the 600 Myr old solar-type Hyades stars of Evensberget et al. (2021), which have $|B_r|$ values about twice as high as χ Dra A. The wind angular momentum loss values for χ Dra A are comparable to the $\dot{J}$ values of Evensberget et al. (2021) and 3–4 times greater than the solar angular momentum loss values found by Finley et al. (2019).

8.3 Wind pressure

Fig. 13 shows the stellar wind pressure in the stellar equatorial plane. The wind density and velocity are affected by local variations in the magnetic field, and this gives rise to spiral arm-like structures. Although the coronal magnetic fields are dipole-like and nearly aligned with the stellar axis of rotation, we observe multiple overdense, high-pressure regions in the stellar equatorial plane. The orbits of a Venus-like, an Earth-like, and a Mars-like planet are shown in Fig. 13 as white dotted circles. The average wind pressure for an Earth-like planet is tabulated in Table 10; these values vary around the average by an order of magnitude due to the presence of the arm-like structures seen in Fig. 13. The average wind pressure values are about 2×10^{-8} Pa which is about 2 times the solar maximum monthly average value, see King & Papitashvili (2005). The magnetospheric stand-off distance for an Earth-like planet, which scales with the sixth root of the wind pressure, can be seen in Table 10 to range from 6.7 to 7.1 planetary radii.

9 DISCUSSION

9.1 Magnetic activity

χ Dra A is a mature (age ∼5 Gyr, Casagrande et al. 2011) late-F star with a wide secondary companion in an ∼280 d orbit. It shows a moderately low level of chromospheric activity (S-Index ∼0.175—0.180). Based on its level of chromospheric activity, and observations of other stars (e.g. Marsden et al. 2014), χ Dra A would be expected to have a moderate longitudinal magnetic field strength, which is the case with a B_l value of ∼ −2.5 to −4.0 G. The absolute value of the longitudinal magnetic field strength of χ Dra A is somewhat stronger than both of the recently studied late-F stars, β Vir, and θ Dra (Seach et al. 2022), even though it has a slower rotation compared to both.

It does not appear that χ Dra has been observed as part of any long-term chromospheric emission monitoring program, such as the Mount Wilson survey (Wilson 1978), thus it is not possible from our data to determine any long-term trends in the chromospheric emission that may be indicative of a magnetic cycle. There is a possible slight increase in the level of chromospheric activity over the ∼5 yr of our observations (Fig. 3) but this is not supported by an increase in the magnitude of the longitudinal magnetic field (Fig.

4), although the error in B_l is significantly larger than that for the Ca II H&K emission measurements (Table 7). We conclude that there appears to be no significant evolution in the magnetic activity of χ Dra A over the ∼5 yr of our observations and, thus, any magnetic cycle would appear to be significantly longer than 5 yr in contrast to some recently studied late-F stars (e.g. τ Boötis, Mengel et al. 2016; Jeffers et al. 2018, and HD 75332, Brown et al. 2021).

9.2 Magnetic maps

The magnetic maps of the large-scale magnetic field of χ Dra A (Figs 5 and 6) show that the star has a relatively stable magnetic field topology over the ∼5 yr of our observations. At all epochs, the radial field has a predominantly negative field in the Northern hemisphere and a positive field in the Southern hemisphere. In contrast to the radial field maps, the azimuthal field maps show consistent regions of positive field centred around the star's equator. The meridional field maps show a weaker mirror of the radial field, which may be due to the cross-talk that ZDI can suffer from for stars with inclination angles significantly over ∼60° (Donati & Brown 1997).

The magnetic parameters (Table 8 and Fig. 9) obtained from the magnetic maps show that the B_{mean} (and B_{max}) values appear to reach a peak for the 2016.63 epoch map, and then decrease again for the 2019.51 map. All maps show a predominantly poloidal magnetic field topology, with the poloidal field accounting for 65^{+6}_{-11} to 90^{+1}_{-3} per cent of the total magnetic field energy. The poloidal field is also predominantly dipolar, with the dipolar percentage ranging from 54^{+12}_{-22} to 74^{+3}_{-14} per cent. During the time of maximum magnetic field, the poloidal percentage is the lowest and the poloidal field is at its most dipolar (although the 'variation' bars for the dipolar percentage are quite large). The epoch of maximum magnetic field strength also corresponds to the lowest level of axisymmetry in the magnetic field, which is to be expected as the toroidal field at this time is more complex (more energy in the $l > 1$ states) and the toroidal field component is the biggest contributor to the axisymmetry of the total field.

These changes are also evident in the maps themselves (Figs 5 and 6), with the stronger and more complex fields appearing on the 2016.63 map. The changes could be due to an evolution of the magnetic field on the surface of χ Dra A, but could also be (at least partly) related to the data quality at each epoch. The data sets have 6 (2014.53), 16 (2015.31), 13 (2016.63), and 12 (2019.51) Stokes V LSD profiles, with SNRs ranging from ∼28 000 to 36 000 (2014.53), ∼27 000 to 45 000 (2015.31), ∼35 000 to 62 000 (2016.63), and ∼14 000 to 70 000 (2019.51). The 2014.53 data set may be the poorest with only six observations, but the other three data sets are reasonably similar to each other in terms of the number of profiles and the SNR. It is possible that the variations in the magnetic field components seen between epochs are real, but the time span between maps is large and the magnitude of variations is small.

We can see in the magnetic maps of χ Dra A (Figs 5 and 6) that there appears to be no strong evidence of a magnetic field reversal, although the 2015.31 map does show a small amount of positive radial field near the Northern pole. All three field components predominantly show the same polarities in each hemisphere at all epochs. Given the complexity and strength of the field in the 2016.63 map, it may be that χ Dra A was approaching activity maximum (although this is not seen in the chromospheric emission) around the middle of 2016 and underwent a polarity reversal shortly after our 2016.63 map. However, if this were the case, then given the similar polarity on the 2014.53 and the 2015.31 maps we would (perhaps naively) expect the 2019.51 map to show a strong (and complex) field
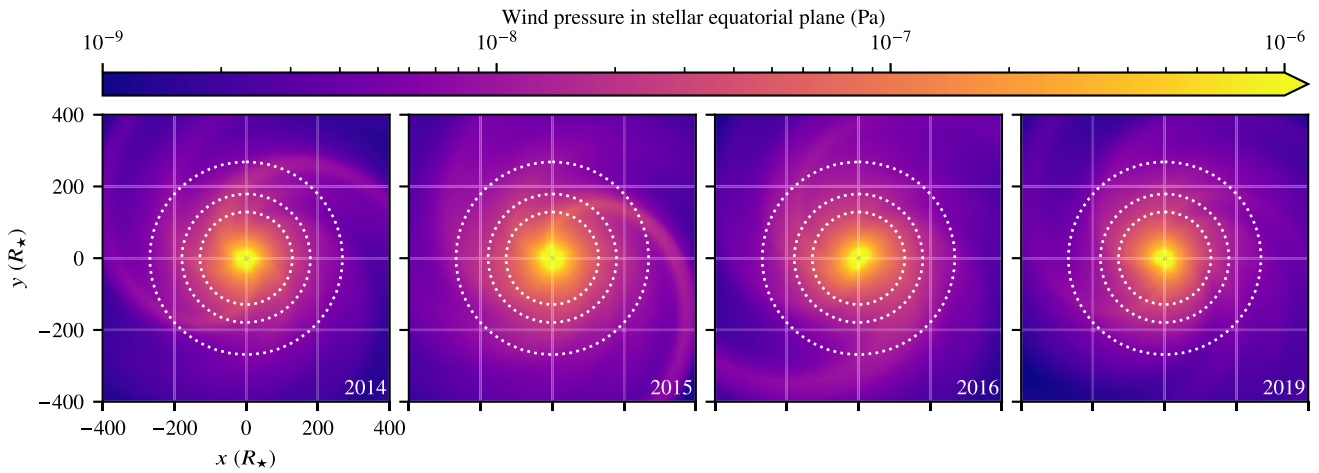
Figure 13. Wind pressure in the stellar equatorial plane. This plot shows the wind pressure in the equatorial plane with the would-be orbits of Venus, the Earth, and Mars indicated by dotted white lines. The intersection of the Alfvén surface and the equatorial plane is indicated by a solid black line. 3–4 armed structures are seen at all epochs.

with a positive (opposite) radial field in the Northern hemisphere, not the weak negative field we see. It could still be that a reversal was missed in this period, but the data suggest this to be unlikely.

Thus it is likely that the magnetic cycle (assuming there is one) for χ Dra A is significantly longer than the ~5 yr of our observations. This is in contrast to some recent observations of mature late-F stars with spectral types very similar to χ Dra A, that appear to show rapid magnetic cycles. The F7V hot Jupiter hosting star τ Boötis was found to have a magnetic polarity reversal every ~120 d (Mengel et al. 2016; Jeffers et al. 2018) and thus a magnetic cycle length of less than a year (~240 d), while Brown et al. (2021) found strong evidence that the (non-hot Jupiter hosting) F7V star HD 75332 has a magnetic reversal every ~193 d, and thus a magnetic cycle length of ~1.06 yr. These are both extremely short compared to the Sun's ~22 yr magnetic cycle, but short cycles appear to be an increasingly common feature of F stars based on their chromospheric emissions, with several stars known to have chromospheric cycle lengths less than a few years (Baliunas et al. 1997; Metcalfe et al. 2010; Mittag et al. 2019; Seach et al. 2022). Thus χ Dra A would appear to be somewhat of an oddity among late-F stars in having a long (if any) magnetic cycle, but further observations would be required to confirm this. χ Dra is a binary and perhaps this could impact any expected magnetic cycle. However, given the long orbital period of the system (~280 d) and a semimajor axis distance of just under 1 au (see Table 6), any interaction between the components appears to be unlikely.

Although Lee et al. (2018) did not create a magnetic map from their observations from late 2006 to late 2008, their longitudinal magnetic field measurements vary from ~ −11 to +11 G, whereas our longitudinal field measurements are always negative, only varying from ~ −1.4 ± 0.5 G to −5.5 ± 0.7 G. Our results are consistent with the predominately poloidal field always having a negative radial field polarity in the Northern (visible) hemisphere (see Figs 5 and 6). The longitudinal magnetic field results from Lee et al. (2018) would tend to indicate that during their observations (in ~2007) χ Dra A had a more complex field structure, and potentially a positive radial magnetic field on the star's Northern hemisphere at some stage. If true, this would indicate that significant changes in the magnetic field topology of χ Dra A can occur, but still does not give any indication of the length of any potential cycle on the star.

9.3 Solid-body rotation

One of the other key findings for late-F stars appears to be a high level of surface differential rotation (e.g. Marsden et al. 2011; Waite et al. 2011) with values often up to 10 times the solar differential rotation rate. However, these results are mainly from younger, often pre-main-sequence stars, rather than mature stars such as χ Dra A. Our results show strong evidence for a zero level of differential rotation (i.e. solid-body rotation) for χ Dra A at all epochs. Measurements of surface differential rotation on mature F stars are more limited compared to younger stars, but the mature hot Jupiter host τ Boötis shows varying levels of surface differential rotation ($d\Omega \sim 0.1$–0.4 rad d^{-1}), all above the solar rate (Mengel et al. 2016; Jeffers et al. 2018). The non-hot Jupiter host HD 75322 also shows a reasonably high level of differential rotation with $d\Omega = 0.25$ rad d^{-1} (Brown et al. 2021). While Reiners & Schmitt (2003) have shown high levels of surface differential rotation on a number of F stars using the Fourier transforms of their line profiles.

Although it is a relatively small sample set, it would appear that once again χ Dra A is unusual with its solid-body rotation. Compared to the other two examples χ Dra is a binary system. However, as mentioned in Section 9.2, given the orbital period of the system is ~280 d with a semimajor axis distance of just under 1 au (Table 6), it would be unlikely that there is significant interaction between the two components, at least at a level that would be expected to impact the rotation of the convective zone of χ Dra A.

9.4 The wind of χ Dra A

The large-scale magnetic maps of χ Dra A (Figs 5 and 6) are relatively stable with the radial magnetic field always showing a dominant dipolar field structure. Thus it is not surprising that the modelling of the coronal field structure (Fig. 11) shows predominantly open field lines at the poles and thus the highest values of wind speed in these polar regions (Fig. 12).

Even though it is a mature star with an age similar to our own Sun, the mass-loss due to the stellar wind from χ Dra A is ~ 3–6 times than that from our own Sun and correspondingly the average wind pressure for a hypothetical Earth in orbit about χ Dra A is ~2 times than that experienced by the Earth due to the Sun. Similarly, the

angular momentum loss from the wind of χ Dra A is 3–4 times that of the Sun (Section 8).

To the authors' knowledge, there are no wind modelling studies that are explicitly focused on F-type stars. There are, however, several wind modelling studies focussing on solar-type (FKG) stars that may include one or more F-type stars. Using a polytropic magnetohydrodynamic approach where the corona is already heated to megakelvin temperatures, Vidotto et al. (2015) modelled the F8V star HD 179949 in a study of solar-type stars, and found a mass-loss value of 5×10^{10} kg s^{-1} and an angular momentum loss value of 2.4×10^{24} Nm. Their mass-loss value is about 5 times higher than the one calculated in this work, while the angular momentum loss value is comparable. Using a similar methodology, Nicholson et al. (2016) modelled the winds of the F7V star τ Boötis at eight different epochs finding mass-loss values of $\sim 1.5 \times 10^{11}$ kg s^{-1} and angular momentum loss values of 1–3×10^{25} Nm. We attribute these particularly high values to the rapid 3-d rotation period of τ Boötis. We do, however, note that the polytropic magnetohydrodynamic (MHD) approach produces higher $\dot{M}$ and $\dot{J}$ values than the Alfvén wave based models used in this work. This can be seen for wind models of solar-type stars using a polytropic approach (Llama et al. 2013; Vidotto et al. 2015; Nicholson et al. 2016; Ó Fionnagáin et al. 2019) compared to the Alfvén wave based methods (Alvarado-Gómez et al. 2016a, b; Pognan et al. 2018; Ó Fionnagáin et al. 2021); see the comparison in Evensberget et al. (2022).

In their study, Alvarado-Gómez et al. (2016b) modelled the G0 star HD 147513 with a 5 d period and found $\dot{M} = 7.2 \times 10^9$ kg s^{-1} and $\dot{J} = 3.7 \times 10^{23}$ N m using an Alfvén wave-based MHD model. These results are similar to the wind model results in this work despite the star's rapid rotation. The study of Pognan et al. (2018) contains wind models of τ Boötis, HD 35296 (F8V), and the G0 star HD 206860. They reported mass-loss values lower by a factor of 2–4 than the ones in this study, while the reported angular momentum loss values are 2–7 times greater. The latter can be expected as these stars are both rapid rotators with 3–5 d rotation periods.

The polytropic and Alfvén based model differences are studied in Cohen (2017) where the authors suggest that polytropic wind models may require calibration to yield realistic winds for not-quite-sunlike stars. This is likely in part because of the view ZDI offers of stellar magnetic fields: In a simulation-based study, Lehmann et al. (2019) found that ZDI recovers the large-scale polarity structure of the stellar magnetic field, but that the field magnitude could not be reliably recovered. Furthermore, the individual features would be reproduced with a magnitude as low as 0.1 of the original magnetic field feature. Similar results have been reported by Yadav et al. (2015), Vidotto et al. (2018), See et al. (2019a), and Kochukhov et al. (2020). The amount of available magnetogram details is also important; Boro Saikia et al. (2020) warned against the uncritical interchange of (detailed) solar magnetogram and the much less detailed ZDI-based stellar magnetograms in wind modelling.

In general, the question of wind model paramter calibration comes up when modelling solar-type stars; this also applies to the solar-calibrated configuration values of the Alfvén wave solar model used in this work. The possible ZDI underreporting of magnetic field strength can be compensated by scaling the magnetic field used to drive the wind models as in the $5B_{\mathrm{ZDI}}$ wind models in Evensberget et al. (2021, 2022) or a similar effect can be achieved through tuning the Alfvén flux-to-field ratio Π_{A}/B (see Table 9). In a study comparing solar and stellar magnetograms, Boro Saikia et al. (2020) found that the Alfvén flux-to-field ratio affects the wind solutions more than the level of detail in the magnetogram, with $\dot{M}$ being roughly proportional to Π_{A}/B. Similar variation should be expected

in $\dot{J}$ values as most theoretical models (e.g. Weber & Davis 1967; Kawaler 1988) predict that $\dot{J} \propto \dot{M}$ (see the values in Table 10).

Recently, Π_{A}/B scaling has been considered by many authors (Garraffo et al. 2016; Dong et al. 2018; Airapetian et al. 2021; Kavanagh et al. 2021; Ó Fionnagáin et al. 2021; Vidotto 2021). The study of Airapetian et al. (2021) in particular applies a strong scaling of $\Pi_{\mathrm{A}}/B \sim 27\,(\Pi_{\mathrm{A}}/B)_{\odot}$ for κ^1 Ceti, a 650 Myr old young Sun proxy (also modelled by do Nascimento et al. 2016 with a polytropic approach) based on far UV observations. Examples such as these show that a variety of wind strengths can achieved through the changing of the model parameters. Consequently the wind models may be most useful in comparing to other wind models obtained via a similar methodology and give insights into trends and variations, rather than be taken as the final word on wind solution properties such as wind pressure, Alfvén surface size, mass-loss, and angular momentum loss. The wind modelling methodology used in this work has previously (Evensberget et al. 2022) shown to be in good agreement with the population study of See et al. (2019b) based on the work of Cranmer & Saar (2011), Finley & Matt (2018), and Matt et al. (2015) as well as the models of Cohen & Drake (2014); this is also the case for the F-type star wind models of this work.

A recent study modelled the wind from two mature late-F stars, the slowly rotating β Vir, and the more rapidly rotating θ Dra (Seach et al. 2022) using an identical methodology to the one of this work. The stellar mass-loss rate and angular momentum loss rate of χ Dra A both fall just above β Vir, while the wind pressure on a hypothetical Earth is more akin to the pressure from the significantly more active and rapidly rotating θ Dra. Thus, despite its moderate rotation, χ Dra A currently appears (based on a very small sample) to have a relatively strong wind for its age and rotation rate. In general, care should be taken when accepting as true the wind mass and angular momentum loss for a single star as the choice of modelling parameters like the Poynting flux-to-field ratio (where we use a Solar value). The wind models presented here are obtained using identical methodology to the wind models of Evensberget et al. (2021, 2022) and Seach et al. (2022) which has permitted a more direct comparison with those works.

Finally, it bears remembering that models of the steady-state wind do not capture mass-loss and angular momentum loss from transient events such as coronal mass ejections and flares.

10 CONCLUSIONS

We have reconstructed the magnetic topology of late-F primary of the χ Dra system at four epochs spanning ~ 5 yr. While there is some indication of slight changes in the magnetic parameters between the epochs, the main structure of the magnetic field does not significantly change over our time-frame, with the field being predominately a dipolar poloidal field at all four epochs.

There is no evidence of any significant magnetic cycle on the star and there are no obvious magnetic polarity reversals during our observations, only a small positive radial field near the pole in the 2015.31 map. Therefore, we conclude that any magnetic cycle on the star is significantly longer than our ~ 5 yr of observations. χ Dra A also appears to rotate as a solid body with a zero level of differential rotation measured for all four epochs. Both of these are in contrast to a number of recent observations of late-F stars.

With our wind modelling parameters, the wind pressure from χ Dra A on a hypothetical Earth is ~ 2 times than that currently

experienced by the Earth, while χ Dra A is losing angular moment at a rate that is ~3–4 times greater than the current solar value.

χ Dra A shows a stable magnetic activity level that appears to be slightly higher than other studied mature late-F stars. There appears to be little evidence of the high levels of surface differential rotation and rapid magnetic cycles seen on other late-F stars. This (along with its extreme brightness) make χ Dra A an interesting target to help our understanding of the magnetic fields of F stars.

DATA AVAILABILITY

All NARVAL data presented here are publicly available through the PolarBase data base (http://polarbase.irap.omp.eu/, Petit et al. 2014). The wind models underlying this article will be shared on reasonable request to the corresponding authors.

REFERENCES

Airapetian V. S. et al., 2020, Int. J. Astrobiol., 19, 136
Airapetian V. S., Jin M., Lüftinger T., Boro Saikia S., Kochukhov O., Güdel M., Van Der Holst B., Manchester W.I., 2021, ApJ, 916, 96
Alecian E., Villebrun F., Grunhut J., Hussain G., Neiner C., Wade G., The BinaMIcS collaboration, 2019, in Brun A. S., Mathis S., Charbonnel C., Dubrulle B., eds, EAS Publ. Ser. Vol. 82, Proceedings of Astro Fluid 2016. EDP Sciences, Les Ulis, France, p. 345
Alfvén H., 1942, Nature, 150, 405
Alvarado-Gómez J. D., Hussain G. A. J., Cohen O., Drake J. J., Garraffo C., Grunhut J., Gombosi T. I., 2016a, A&A, 588, A28
Alvarado-Gómez J. D., Hussain G. A. J., Cohen O., Drake J. J., Garraffo C., Grunhut J., Gombosi T. I., 2016b, A&A, 594, A95
Aurière M., 2003, in Arnaud J., Meunier N., eds, EAS Publ. Ser. Vol. 9, Magnetism and Activity of the Sun and Stars. EDP Sciences, Les Ulis, France, p. 105
Baliunas S. L. et al., 1995, ApJ, 438, 269
Baliunas S. L., Henry G. W., Donahue R. A., Fekel F. C., Soon W. H., 1997, ApJ, 474, L119
Baschek B., Reimers D., 1969, A&A, 2, 240
Berdyugina S. V., 2005, Living Rev. Sol. Phys., 2, 8
Böhm-Vitense E., Dettmann T., 1980, ApJ, 236, 560
Boro Saikia S. et al., 2016, A&A, 594, A29

Boro Saikia S., Jin M., Johnstone C. P., Lüftinger T., Güdel M., Airapetian V. S., Kislyakova K. G., Folsom C. P., 2020, A&A, 635, A178
Borsa F. et al., 2015, A&A, 578, A64
Bouvier J., Matt S. P., Mohanty S., Scholz A., Stassun K. G., Zanni C., 2014, in Beuther H., Klessen R. S., Dullemond C. P., Henning T., eds, Protostars and Planets VI. University of Arizona Press, Tucson, p. 433
Brown E. L. et al., 2021, MNRAS, 501, 3981
Brun A. S., Browning M. K., 2017, Living Rev. Sol. Phys., 14, 4
Casagrande L. et al., 2011, A&A, 530, A138
Cohen O., 2017, ApJ, 835, 220
Cohen O., Drake J. J., 2014, ApJ, 783, 55
Čokina M., Fedurco M., Parimucha Š., 2021, A&A, 652, A156
Cranmer S. R., Saar S. H., 2011, ApJ, 741, 54
do Nascimento J.-D. Jr et al., 2016, ApJ, 820, L15
Donati J.-F. et al., 2006, MNRAS, 370, 629
Donati J.-F., Brown S. F., 1997, A&A, 326, 1135
Donati J.-F., Landstreet J. D., 2009, ARA&A, 47, 333
Donati J.-F., Semel M., Carter B. D., Rees D. E., Collier Cameron A., 1997, MNRAS, 291, 658
Dong C., Jin M., Lingam M., Airapetian V. S., Ma Y., van der Holst B., 2018, Proc. Natl. Acad. Sci., 115, 260
Evensberget D., Carter B. D., Marsden S. C., Brookshaw L., Folsom C. P., 2021, MNRAS, 506, 2309
Evensberget D., Carter B. D., Marsden S. C., Brookshaw L., Folsom C. P., Salmeron R., 2022, MNRAS, 510, 5226
Fares R. et al., 2012, MNRAS, 423, 1006
Farrington C. D. et al., 2010, AJ, 139, 2308
Finley A. J., Deshmukh S., Matt S. P., Owens M., Wu C.-J., 2019, ApJ, 883, 67
Finley A. J., Matt S. P., 2018, ApJ, 854, 78
Folsom C. P. et al., 2018, MNRAS, 474, 4956
Fossati L. et al., 2015, A&A, 582, A45
Gallet F., Bouvier J., 2015, A&A, 577, A98
Gallet F., Charbonnel C., Amard L., Brun S., Palacios A., Mathis S., 2017, A&A, 597, A14
Garraffo C. et al., 2018, ApJ, 862, 90
Garraffo C., Drake J. J., Cohen O., 2016, ApJ, 833, L4
Gombosi T. I., van der Holst B., Manchester W. B., Sokolov I. V., 2018, Living Rev. Sol. Phys., 15, 4
Gray D. F., 1984, ApJ, 281, 719
Gray R. O., Napier M. G., Winkler L. I., 2001, AJ, 121, 2148
Grunhut J. H. et al., 2017, MNRAS, 465, 2432
Grunhut J. H., Neiner C., 2015, in Nagendra K. N., Bagnulo S., Centeno R., Jesús Martínez González M., eds, Proc. IAU Symp. 305, Polarimetry. Kluwer, Dordrecht, p. 53
Grunhut J. H., Wade G. A., MiMeS Collaboration, 2012, in Drissen L., Robert C., St-Louis N., Moffat A. F. J., eds, ASP Conf. Ser. Vol. 465, Proceedings of a Scientific Meeting in Honor of Anthony F. J. Moffat. Astron. Soc. Pac., San Francisco, p. 42
Hall J. C., 2008, Living Rev. Sol. Phys., 5, 2
Hunter J. D., 2007, Comput. Sci. Eng., 9, 90
Iglesias-Marzoa R., López-Morales M., Morales M., 2015, PASP, 127, 567
Jeffers S. V. et al., 2018, MNRAS, 479, 5266
Jeffers S. V. et al., 2022, A&A, 661, A152
Jenkins J. M. et al., 2016, in Chiozzi G., Guzman J. C., eds, Proc. SPIE Conf. Ser. Vol. 9913, Software and Cyberinfrastructure for Astronomy IV. SPIE, Bellingham, p. 1232
Johnstone C. P., Khodachenko M. L., Lüftinger T., Kislyakova K. G., Lammer H., Güdel M., 2019, A&A, 624, L10
Kavanagh R. D., Vidotto A. A., Klein B., Jardine M. M., Donati J.-F., Ó Fionnagáin D., 2021, MNRAS, 504, 1511
Kawaler S. D., 1988, ApJ, 333, 236
King J. H., Papitashvili N. E., 2005, J. Geophys. Res., 110, A02104
Kochukhov O., Hackman T., Lehtinen J. J., Wehrhahn A., 2020, A&A, 635, A142
Kochukhov O., Makaganiuk V., Piskunov N., 2010, A&A, 524, A5
Lammer H. et al., 2010, Astrobiology, 10, 45

Landi E., Young P. R., Dere K. P., Del Zanna G., Mason H. E., 2013, ApJ, 763, 86

Landstreet J. D., 1992, A&AR, 4, 35

Lee B.-C. et al., 2018, MNRAS, 473, L41

Lehmann L. T., Hussain G. A. J., Jardine M. M., Mackay D. H., Vidotto A. A., 2019, MNRAS, 483, 5246

Linker J. A. et al., 2017, ApJ, 848, 70

Llama J., Vidotto A. A., Jardine M., Wood K., Fares R., Gombosi T. I., 2013, MNRAS, 436, 2179

Luck R. E., 2017, AJ, 153, 21

Marsden S. C. et al., 2011, MNRAS, 413, 1939

Marsden S. C. et al., 2014, MNRAS, 444, 3517

Marsden S. C., Mengel M. W., Donati F., Carter B. D., Semel M., Petit P., 2006, in Casini R., Lites B., ed., Solar Polarization 4, Vol. 358. Astron. Soc. Pac., San Francisco, p. 401

Martínez-Arnáiz R., Maldonado J., Montes D., Eiroa C., Montesinos B., 2010, A&A, 520, 79

Matt S. P., Brun A. S., Baraffe I., Bouvier J., Chabrier G., 2015, ApJ, 799, L23

Matt S. P., MacGregor K. B., Pinsonneault M. H., Greene T. P., 2012, ApJ, 754, L26

Meng X., van der Holst B., Tóth G., Gombosi T. I., 2015, MNRAS, 454, 3697

Mengel M. W. et al., 2016, MNRAS, 459, 4325

Mengel M. W., 2005, Master of philosophy thesis, University of Southern Queensland

Messina S. et al., 2016, A&A, 596, A29

Mestel L., 1968, MNRAS, 138, 359

Metcalfe T. S. et al., 2022, ApJ, 933, L17

Metcalfe T. S., Basu S., Henry T. J., Soderblom D. R., Judge P. G., Knölker M., Mathur S., Rempel M., 2010, ApJ, 723, L213

Mishra W., Srivastava N., Wang Y., Mirtoshev Z., Zhang J., Liu R., 2019, MNRAS, 486, 4671

Mittag M., Schmitt J. H. M. M., Hempelmann A., Schröder K.-P., 2019, A&A, 621, 136

Morgenthaler A., Petit P., Morin J., Aurière M., Dintrans B., Konstantinova-Antova R., Marsden S., 2011, Astron. Nachr., 332, 866

Neiner C., Mathis S., Alecian E., Emeriau C., Grunhut J., BinaMIcS Collaborations, 2015, in Nagendra K. N., Bagnulo S., Centeno R., Jesús Martínez González M., eds, Proc. IAU Symp. 305, Polarimetry. Kluwer, Dordrecht, p. 61

Neiner C., Wade G. A., Marsden S. C., Blazère A., 2017, in Zwintz K., Poretti E., eds, PAS Conf. Ser. Vol. 5, Second BRITE-Constellation Science Conference: Small satellites—big science. Pol. Astron. Soc., Warsaw, p. 86

Nicholson B. A. et al., 2016, MNRAS, 459, 1907

Ó Fionnagáin D. et al., 2019, MNRAS, 483, 873

Ó Fionnagáin D., Vidotto A. A., Petit P., Neiner C., Manchester W.I., Folsom C. P., Hallinan G., 2021, MNRAS, 500, 3438

Oran R., Van Der Holst B., Landi E., Jin M., Sokolov I. V., Gombosi T. I., 2013, ApJ, 778, 176

Pace G., 2013, A&A, 551, L8

Petit P. et al., 2021, A&A, 648, A55

Petit P., Donati J.-F., Collier Cameron A., 2002, MNRAS, 334, 374

Petit P., Louge T., Théado S., Paletou F., Manset N., Morin J., Marsden S. C., Jeffers S. V., 2014, PASP, 126, 469

Pognan Q., Garraffo C., Cohen O., Drake J. J., 2018, ApJ, 856, 53

Reiners A., 2012, Living Rev. Sol. Phys., 9, 1

Reiners A., Schmitt J. H. M. M., 2003, A&A, 398, 647

Rice J. B., 2002, Astron. Nachr., 323, 220

Ricker G. R. et al., 2014, in Oschmann Jr J. M., Clampin M., Fazio G. G., MacEwen H. A., eds, Proc. SPIE Conf. Ser. Vol. 9143, Space Telescopes and Instrumentation 2014: Optical, Infrared, and Millimeter Wave. SPIE, Bellingham, p. 556

Ridgway R. J. et al., 2023, MNRAS, 518, 2472

Riley P., Lionello R., Caplan R. M., Downs C., Linker J. A., Badman S. T., Stevens M. L., 2021, A&A, 650, A19

Roussev I. I. et al., 2003, ApJ, 595, L57

Sachdeva N. et al., 2019, ApJ, 887, 83

Schatten K. H., 1971, Cosm. Electrodyn., 2, 232

Schofield M. et al., 2019, ApJS, 241, 12

Schöller M. et al., 2017, A&A, 599, A66

Seach J. M., Marsden S. C., Carter B. D., Evensberget D., Folsom C. P., Neiner C., Mengel M. W., 2022, MNRAS, 509, 5117

Seach J. M., Marsden S. C., Carter B. D., Neiner C., Folsom C. P., Mengel M. W., Oksala M. E., Buysschaert B., 2020, MNRAS, 494, 5682

See V. et al., 2018, MNRAS, 474, 536

See V. et al., 2019a, ApJ, 876, 118

See V. et al., 2019b, ApJ, 886, 120

See V., Jardine M., Vidotto A. A., Petit P., Marsden S. C., Jeffers S. V., do Nascimento J. D. Jr, 2014, A&A, 570, A99

Semel M., 1989, A&A, 225, 456

Shoda M. et al., 2020, ApJ, 896, 123

Skumanich A., 1972, ApJ, 171, 565

Soderblom D. R., Jones B. F., Fischer D., 2001, ApJ, 563, 334

Sokolov I. V. et al., 2013, ApJ, 764, 23

Swinbank R., Purser R. J., 2006, Q. J. R. Meteorol. Soc., 132, 1769

Takeda G., Ford E. B., Sills A., Rasio F. A., Fischer D. A., Valenti J. A., 2007, ApJS, 168, 297

ten Brummelaar T. A. et al., 2005, ApJ, 628, 453

Tomkin J., Mcalister H. A., Hartkopf W. I., Fekel F. C., 1987, AJ, 93, 1236

Torres G., Andersen J., Giménez A., 2010, A&AR, 18, 67

Tóth G. et al., 2005, J. Geophys. Res., 110, A12226

Tóth G. et al., 2012, J. Comput. Phys., 231, 870

van der Holst B., Manchester IV W. B., Klein K. G., Kasper J. C., 2019, ApJ, 872, L18

van der Holst B., Sokolov I. V., Meng X., Jin M., Manchester W. B., Gombosi T. I., 2014, ApJ, 782, 81

van der Walt S., Colbert S. C., Varoquaux G., 2011, Comput. Sci. Eng., 13, 22

Vidotto A. A., 2021, Living Rev. Sol. Phys., 18, 3

Vidotto A. A., Cleary A., 2020, MNRAS, 494, 2417

Vidotto A. A., Fares R., Jardine M., Moutou C., Donati J.-F., 2015, MNRAS, 449, 4117

Vidotto A. A., Lehmann L. T., Jardine M., Pevtsov A. A., 2018, MNRAS, 480, 477

Virtanen P. et al., 2020, Nat. Methods, 17, 261

Wade G. A. et al., 2016, MNRAS, 456, 2

Waite I. A., Marsden S. C., Carter B. D., Hart R., Donati J. F., Ramírez Vélez J. C., Semel M., Dunstone N., 2011, MNRAS, 413, 1949

Waite I. A., Marsden S. C., Carter B. D., Petit P., Donati J.-F., Jeffers S. V., Boro Saikia S., 2015, MNRAS, 449, 8

Weber E. J., Davis L., 1967, ApJ, 148, 217

Weiss W. W. et al., 2014, PASP, 126, 573

Wilson O. C., 1966, ApJ, 144, 695

Wilson O. C., 1978, ApJ, 226, 379

Wright J. T., Marcy G. W., Butler R. P., Vogt S. S., 2004, ApJS, 152, 261

Yadav R. K., Christensen U. R., Morin J., Gastine T., Reiners A., Poppenhaeger K., Wolk S. J., 2015, ApJ, 813, L31

Zechmeister M., Kürster M., 2009, A&A, 496, 577

APPENDIX: GENERALIZED LOMB–SCARGLE ANALYSIS

For the Ca II HK activity (Section 4), longitudinal magnetic field measurements (Section 5), and *TESS* photometry (Section 7), we undertook a generalized Lomb–Scargle analysis (Zechmeister & Kürster 2009) to look for evidence of a rotational period for χ Dra A. No period was found with the results shown in Figs A1, A2, and A3.
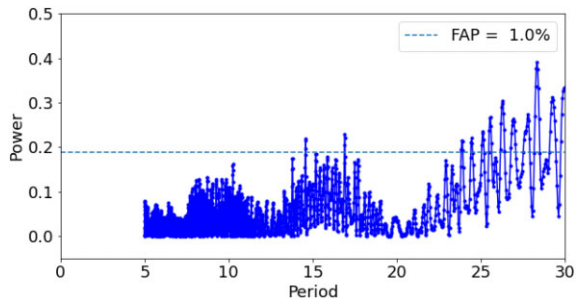
Figure A1. Generalized Lomb–Scargle analysis of the χ Dra Ca II HK activity. with a false-alarm probability of 1.0 per cent shown as the dashed line.
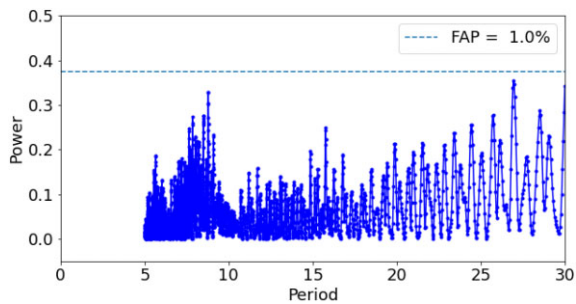

Figure A3. As Fig. A1, but for the *TESS* photometry of χ Dra.

Figure A2. As Fig. A1, but for the longitudinal magnetic field of χ Dra A.

This paper has been typeset from a TEX/LATEX file prepared by the author.